Title
Design of an Insect-Scale Flapping-Wing Robot with Concomitant Piezoelectric Velocity Sensing for Flight

Author
Lan, Edward I

Publication Date
2022

Peer reviewed|Thesis/dissertation

UNIVERSITY OF CALIFORNIA SAN DIEGO

Design of an Insect-Scale Flapping-Wing Robot with Concomitant Piezoelectric Velocity Sensing for Flight

A Thesis submitted in partial satisfaction of the requirements
for the degree Master of Science

in

Engineering Sciences (Mechanical Engineering)

by

Edward Lan

Committee in charge:

Professor Nicholas Gravish, Chair
Professor Shengqiang Cai
Professor Michael Tolley

2022

The Thesis of Edward Lan is approved, and it is acceptable in quality and form for publication on microfilm and electronically.

University of California San Diego

2022

DEDICATION

To my Family, Evans, Charlene and David. To my Girlfriend Doris, and to all my friends and colleagues who have helped me get to where I am today, and will be tomorrow.

TABLE OF CONTENTS

LIST OF FIGURES

LIST OF TABLES

LIST OF ABBREVIATIONS

FWMAV	Flapping-Wing Micro-Aerial Vehicle
PEA	Piezoelectric Actuator

ACKNOWLEDGEMENTS

Significant thanks to Professor Nicholas Gravish for advising and providing significant feedback for this project. Additionally, many thanks to the members of the Flapping-Wings Topic group in the Gravishlab, James Lynch, Hang Gao, and David Zhu, for providing worthwhile criticisms and for helping to push the boundaries of flapping-wing robotic flight. Finally, many thanks go out to all the members of Gravishlab, who have contributed in helpful discussion to move this project forwards.

Chapter 1 remarks on a DSA transfer function, which is the direct work of James Lynch, and it was due to his help and guidance, that this research, and the results found, were able to come to fruit. Chapter 1 is currently being prepared for submission for publication. Lan, Edward; Lynch, James; Gravish, Nicholas. "Controlled Flight of a Bioinspired Flapping Wing Robot with Asynchronous Control". The thesis author was the principle researcher/author on this paper.

ABSTRACT OF THE THESIS

Design of an Insect-Scale Robot and Concomitant Piezoelectric Velocity Sensing for Flapping-Wing Flight

by

Edward Lan

Engineering Sciences (Mechanical Engineering)

University of California San Diego, 2022

Professor Nicholas Gravish, Chair

Current bioinspired flapping-wing micro aerial robots incorporate numerous capabilities pulled from the study of insect morphologies, and have utilized these designs to improve flight stability, time, and energy efficiency. However, this approach to the design of robotic systems draws unidirectionally from the threshold of biology into robotics, pulling from mechanisms that evolutionary biology has spent millennia iterating, without utilizing these robots to further study insect and animal traits. In this research we develop a flapping-wing micro-aerial robot, scaled up in size from the Harvard RoboBee, designed as a platform for studying the control mechanisms inherent in insect muscle physiology. A concomitant velocity sensing circuit is implemented in a piezoelectric actuator, to self-sense the velocity of the actuator tip and feed it into a control feedback loop. The loop simulates antagonistic delay-stretch activation muscles, mimicking insects that fly asynchronously. Using concomitant sensing and the flapping-wing robot, the system generates stable oscillatory flapping-wing motion without the use of large off-board displacement sensors across a range of control parameters, and performs as a platform for future DSA control studies.

INTRODUCTION

Bioinspired design of robots capable of flapping-wing flight, have focused on understanding and mimicking the mechanics and energetics of flapping-wing creatures, and have resulted in amazing robots such as the Aerovironment Nano Hummingbird, the Harvard RoboBee, and the Harvard RoboBee X-wing. These systems integrate key mechanisms of biological systems to produce energetically favorable flight capabilities, and sometimes exceed the energetic efficiencies of their natural counterparts. In this way, biology provides designs that generate interesting and useful mechanisms in robotics, but this unidirectional application of bioinspired design has not extended itself to further studying the creatures it may be based on. To this end, it seems that a bioinspired robot, based upon a biological system, could be utilized to further study interesting properties of the original creature, and could provide discoveries and beneficial improvements to existing bioinspired designs in a more symbiotic relationship.

The study of the control systems that exist in the muscle morphologies of asynchronous flapping-wing insects provides an avenue for which to perform this more symbiotic relationship of bioinspired design to biological study. Utilizing a flapping-wing robot whose method of locomotion is based upon the same motions and properties of micro-scale flight, feedback loops can be implemented that mimic muscle control systems in winged insects. Delay-stretch activated (DSA) muscles, which are inherent in the physiology of insects that perform asynchronous flight, are a particularly intriguing area of focus, as it has been suggested that the antagonistic muscle-pairs can be translated into a transfer function and used in conjunction with an actuator and sensor to generate stable oscillatory motions that can be tuned for flight in a robotic system.

CHAPTER 1: BACKGROUND

SECTION 1.1 FLAPPING-WING FLIGHT AND BIOINSPIRED DESIGN

Flapping-wing aerial robots capable of autonomous flight have become a highly sought technology in recent decades as an option for remotely operated robots capable of accessing a variety of environments that could be unsuitable for human interaction. The benefits of flapping-wing flight for smaller scale robots includes energy preservation and higher efficiency at low Reynolds numbers (<1000)[1] as compared to rotor-type flying vehicles which utilize electromagnetic motors as a power source. Additionally, flapping wing robots allow for unique flight control capabilities[2] and low acoustic signatures[3], making them particularly interesting from a reconnaissance standpoint. Breakthroughs in Flapping Wing Micro-Aerial Vehicles (FWMAVs) research have had foundations in bioinspired design, utilizing flapping wing insects as a framework for flapping wing robots. These breakthroughs continue to push the field closer towards achieving lightweight robots with on-board control and power autonomy.

Bioinspired flapping-wing robots mimic insect wing motions, such as that of bees, to generate vertical lift. The wing motion of a bee’s wings can be seen in Figure 4, and consists of 2 main movements. The first movement acts along the horizontal plane, in which the wing performs a stroke, bringing its wingtip back and forth along the horizontal plane. The second movement involves pitching of the wing along a pivot axis, running along the top of the wing. The wing pitches during the stroke, pushing air in a diagonally downwards direction, generating an opposite and equal reaction force from the air drag that acts as the vertical lift of the insect. At high frequencies of flapping, this motion occurs on the order of anywhere from 30Hz to 2000Hz, continually generating forces in a downward direction that allow the insect to hover and fly.

Slight deviations in the motions on either wing side generate asymmetric forces that translate into pitch, yaw, and roll, and are necessary for orientation control and lateral movement.

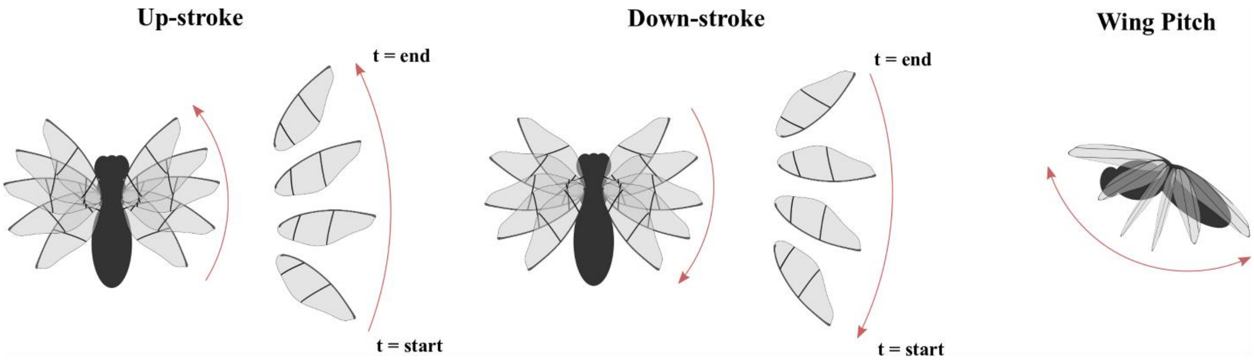

Figure 1. Wing path of a bee includes lateral stroke (Up-stroke and Down-stroke) Combined with wing pitch

Bioinspired FWMAVs rely on a combination of a passive wing pitching with forced lateral wing sweeps to generate vertical lift forces. As the wing laterally sweeps along the horizontal plane, a passive hinge allows the wing to angle itself due to air drag. The angled wing generates a directional force that has a component that pushes air in a downward direction, generating lift. In this configuration, the pitch angle of the wing relative to the stroke is extremely important, as improper phasing of the two can cost valuable vertical forcing through the period of stroke.

A multitude of mechanical and design factors play into the generation of lift for an insect, including wing pitch angle, stroke amplitude, frequency of wing stroke, wing shape and wing inertia. Studies have shown that certain wing shapes are beneficial for different types of insect flight and motion, and that the mechanical properties of these systems have been tuned by nature over millennia, to produce insects capable of controlled flapping wing flight. It has been theorized that insects utilize the natural mechanical resonance of their muscular and wing systems to generate efficient vertical lift. This has been shown in studies[4], and has been a focal design point in developing flapping wing robots, such that systems that are designed for this method of flight are often designed and built to tune the resonance of the flapping stroke and pitch angle based on characteristics of mass and stiffness of the system.

Elastic materials in the muscles of the insects provide highly efficient antagonistic motion[5], which allows for minimal loss in energy due to the wing reaching its mechanical end stroke[6]. It has also been discovered that insects' muscular design and attributes contribute to the overall efficiency of their flight capabilities. Utilizing compliant and elastic materials, bioinspired flapping wing robots generate increased lift efficiencies, like insects[7], [8].

SECTION 1.2 FLAPPING-WING ROBOTS

The use of bio-inspired design for flapping wing flight has allowed for the development of robots such as the Harvard MoBee[9], RoboBee[2], and RoboBee X-Wing[10], as well as Aerovironment's Nano hummingbird[11] shown in Figure 2. These systems have proven that it is possible to develop flapping wing systems capable of generating controlled lift in various forms.

Limitations on these designs are often related to power and energy constraints and control and sensing constraints. Current robotic solutions utilize "tethers" to provide a conduit for power and control signal implementation. Large off-board power sources are required to provide sufficient energy to lift the robot up and perform flight maneuvers. Similarly, control computers are currently required to be off-boarded to provide sufficiently fast computation of flight sensor data to then generate a control input to control the position and motion of the robots.

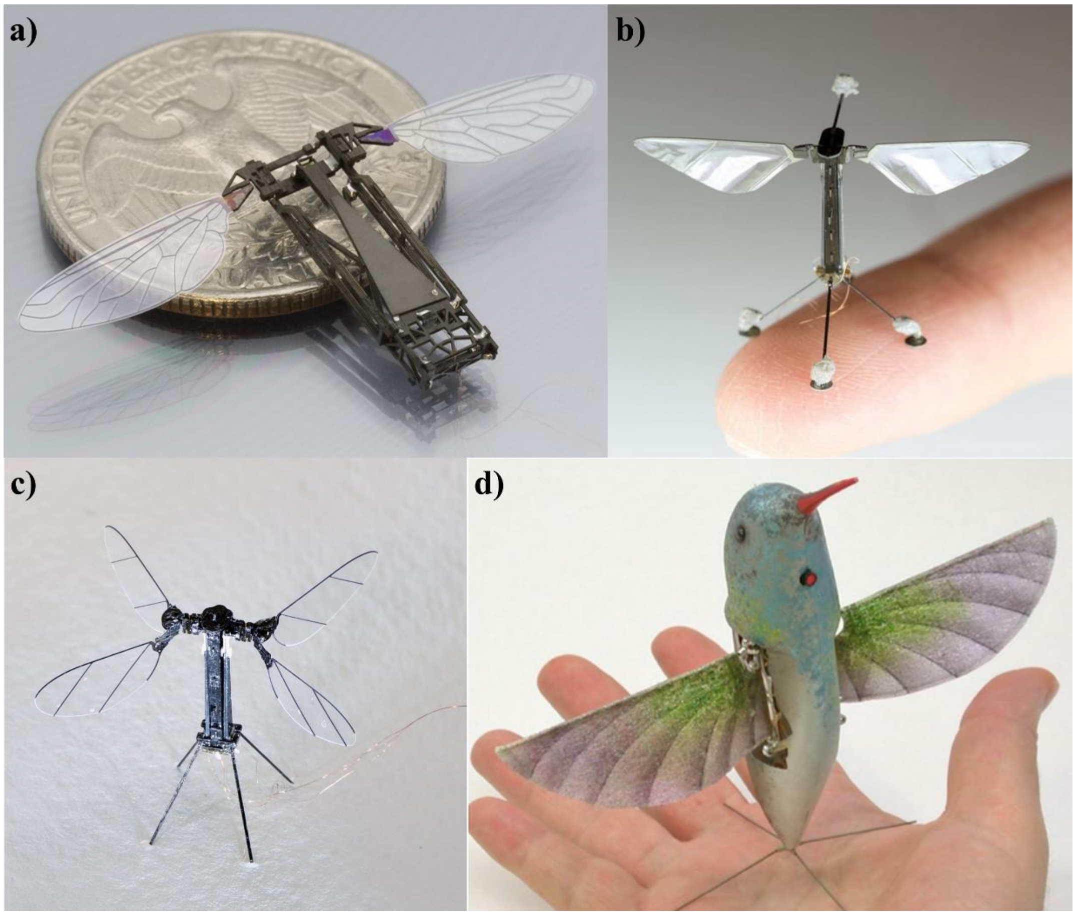

Figure 2. a) Mobee[9] b) RoboBee[2] c) RoboBee X-Wing[10] d) Nano Hummingbird[11]

SECTION 1.3 ASYNCHRONOUS INSECT FLIGHT AND DSA MUSCLES

Asynchronous flight muscles, or fibrillar or myogenic muscles, are muscle sets that exhibit asynchrony between the electrical impulses from the brain and the muscle's contractions[12], [13]. Insects with asynchronous flight muscles provide a neural input which generates an oscillatory contraction response that generates high frequency flapping wing motion. In comparison, synchronous muscles exhibit a 1:1 ratio of neural input to muscle contraction, and while they allow for a more direct control paradigm, they also require an exhaustive amount of neural load for high frequency motion.

To induce this type of high frequency oscillatory response, insects utilize antagonistic sets of delay-stretch-activation muscles which provide counteracting contractions to generate these oscillatory motions. As one pair of muscles activates it pulls the antagonistic muscle in such a way that it stretches it. After a delay, when the first antagonistic muscle has deactivated, the second muscle pair will activate, due to its stretch-activation properties, and contract. This contraction then generates a stretch in the second pair of muscles and the cycle repeats in an oscillatory fashion.

This method of minimizing neural load for high frequency motion is one of the mechanisms that provides insects with the capability for flight despite their small mass and large energy requirements. Approximately three quarters of insects have been shown to utilize these asynchronous muscles for flight[12] and energy efficiency of flapping wing oscillations. This method of flapping wing flight generation provides a unique control method that can be implemented in FWMAVs to generate higher efficiency flight capabilities, and to possibly allow for interesting flight features such as impact recovery and lower frequency control requirements for sustained flight. In the research presented, a formation of the DSA muscle, computed as a transfer function, was utilized as a method of autonomous flapping wing frequency control. The transfer function was defined as:

$$G(s) = \frac{r_3 - r_4}{s^2 + (r_3 + r_4)s + r_3 r_4}$$

Where:

$$r_4 = r_3 \kappa$$

In this transfer function, r_3 and $r_4$are parameters that affect the delay-stretch activation parameters of the system, and κ is a ratio that defines the relationship between the r_3 and $r_4$parameters. In our research we utilize a κ of 0.62, which has been found to be approximately similar to that of a Hawkmoth. Thus we are able to vary a single variable r_3 to affect the delay-stretch activated properties of the control system. A gain term μ is also added which scales the system, and is used to tune stable oscillatory modes. Thus, given the ability to change r_3 and μ, we are able to fully tune the system to generate stable oscillations.

SECTION 1.4 POP-UP MEMS

To build flying micro-robots, there is an inherent need to utilize materials with low mass to stiffness ratios to prevent unstable vibrations within the structure of the robot itself. To this degree, a method of fabrication known as pop-up book MEMs has been developed that utilizes thin carbon fiber laminates (3-5 unidirectional plies), polyimide film (Kapton®), and thermal adhesive to create foldable structures for flapping wing micro-robots[14]. This process has been implemented in a variety of micro-robots, from micro-scale medical robots[15], [16], to legged insect robots[17]–[19], to flapping wing robots[2], [9], [20].

Fabrication using this method utilizes laser micromachining of thin bondable sheets of various materials to remove cutouts from a blank to define structural features in the final part. Once the layers are cut, they are aligned and heat-pressed using a fixture and precision pins. Under 30+ psi of pressure, the stack-up is heated to 350F to allow layers of thermal adhesive film to melt and bond the substrate layers, connecting layers of carbon fiber, polyimide film, copper, and or fiberglass together. When the stack-up has fully cured, it is then micro-machined again to release the component from the alignment structure. The released part can then be folded and glued into a final assembly structure for any parts requiring manipulation into a complex shape. A process diagram is shown in Figure 3, which shows the fabrication process for a transmission.

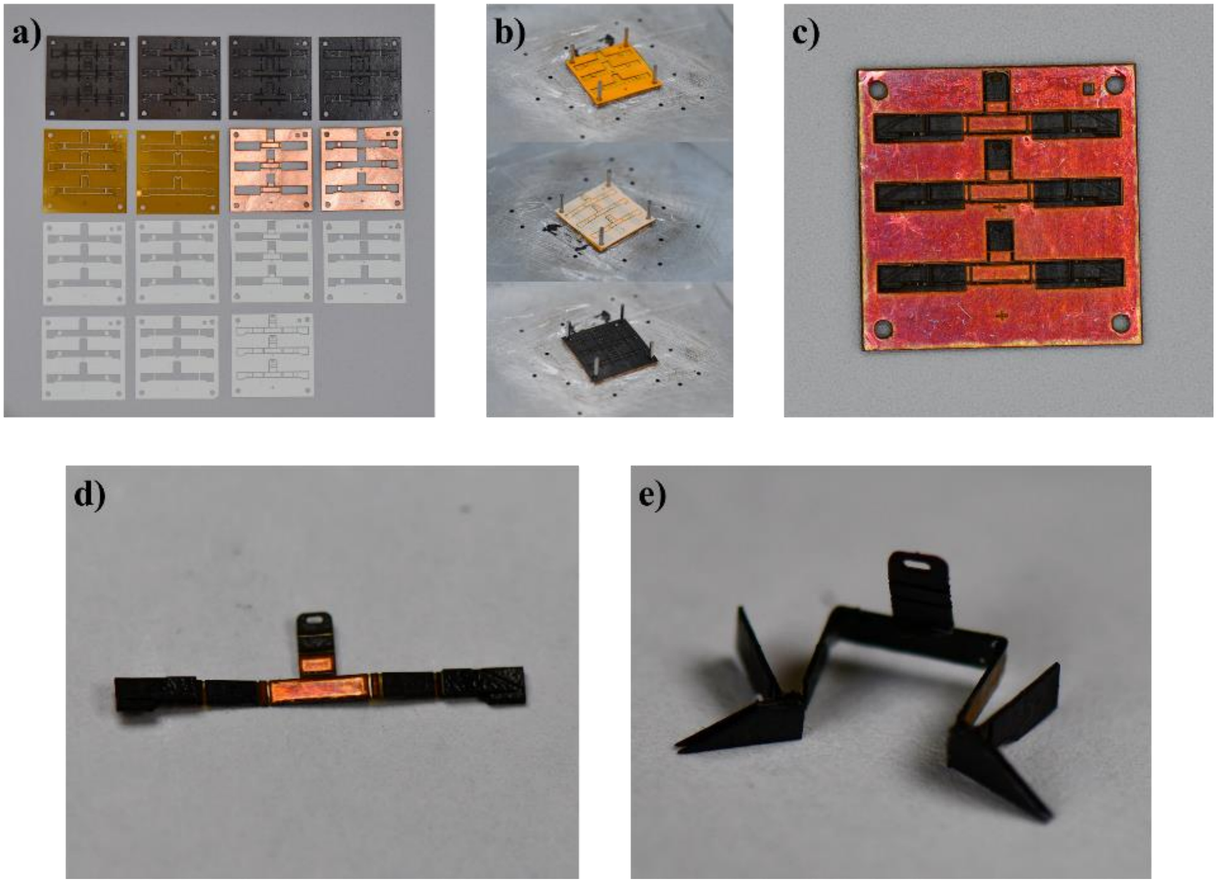

Figure 3. Pop-Up Mems Fabrication Process - a) Layers of Carbon Fiber/Polyimide Film/Copper/Thermal Adhesive Are Micromachined Using a DPSS Laser b) Layers of Cut Material are Stacked up on Alignment Jig c) Stack is Cured under 350F Thermal Load At 30 PSI for 2 Hours d) Final Component is Release Cut using DPSS Laser e) Component is Folded and Cyanoacrylate Glue applied to form the rigid junctions and final Shape

SECTION 1.5 PIEZOELECTRIC ACTUATORS

With the miniaturization of robots comes an added benefit from utilizing a flapping wing design that does not require a magnetic coil-driven rotational motor, but instead utilizes a higher efficiency piezoelectric actuator (PEA). As the size of the commonly used DC motor decreases, so does its power to mass and power to volume efficiency[21]. As the size of common electromagnetic motor decreases, more and more of the structure becomes parasitic mass that does not contribute to the overall flight capabilities of the vehicle. In comparison, use of a PEA, which is easily adapted to flapping wing flight through a compliant transmission, as seen in multiple instances of bioinspired FWMAVs, allows for better energy and power efficiencies[21] at such size scales.

Piezoelectric ceramic materials are ceramics that exhibit strain when an electrical load is applied. These materials have a wide range of applications but are mostly suited to operations that require fast and precise controlled motion. PEAs are particularly effective in smaller volume and mass constraints as opposed to more common electromagnetic motors for actuation. Due to scaling effects, the power density of the actuator has been shown to increase with decreased size and at higher frequencies of motion[21], [22].

Piezo ceramics are classified by their electrical and mechanical and thermal properties, to produce desired mechanical operations under a given set of environmental conditions. For higher stability at a wider range of temperatures, Navy type III (PZT-5H), provides stable operations within a large temperature regime. This was chosen as the material type for the piezoelectric actuator due to its stability under a varying number of conditions. This allows the actuator and subsequently, the robot, to eventually operate under a wide array of conditions as can be felt in a natural environment.

PEAs come in many shapes, for both linear and rotational motion. The actuator type used for the purposes of this research was a tri-morph actuator, which is composed of two (2) piezo ceramic plates aligned in their polarization, with a layer of conductive carbon fiber stacked in between as seen in Figure *4*.

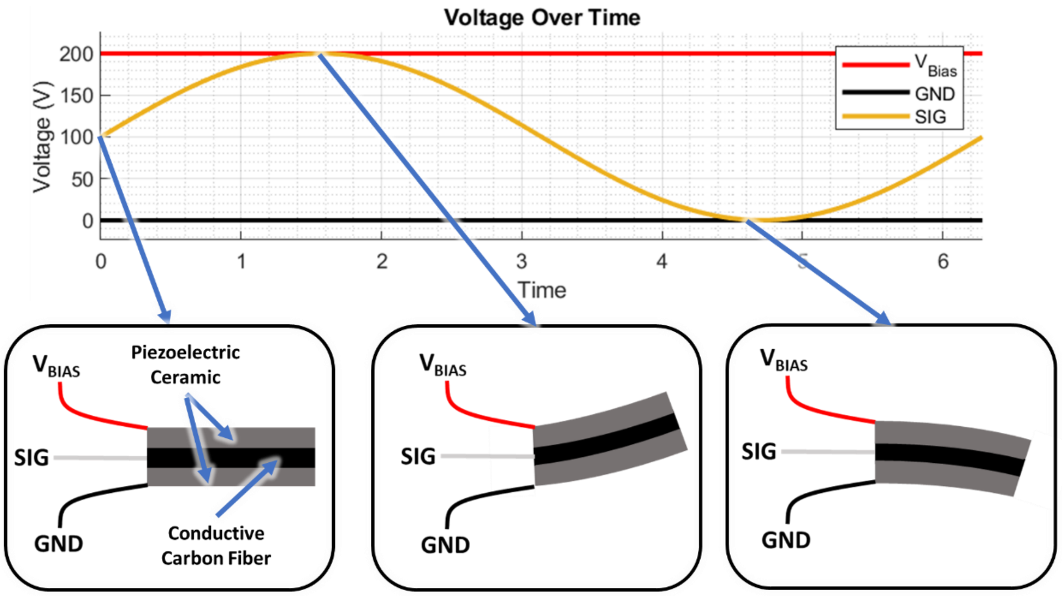

Figure 4. A piezoelectric tri-morph is composed of two (2) layers of piezoelectric ceramic and one (1) layer of conductive carbon fiber generate beam bending as electric potential is varied along the signal (SIG) input line

The method of motion for a trimorph piezoelectric actuator is such that a bias voltage is held along the top layer of the topmost piezoceramic layer, and a ground voltage is held at the bottom of the lowest piezoceramic layer. The carbon fiber layer then has a signal voltage applied which lies between the ground and bias voltages and causes potential differences between the outer layers of the piezoceramics and the layers which contact the carbon fiber directly. As the signal changes, the potential difference across the carbon fiber layer axis generates different strains along the opposing piezoceramic layers as shown in Figure *4*. When fixed as a clamped-free bending cantilever, the actuator elongates along the longitudinal direction to produce beam-bending.

SECTION 1.6 CONCOMITANT SENSING

To generate feedback controls for flapping wing robots, it is necessary to provide capabilities for sensing in the robot. In the case of the controlled flight of the Harvard RoboBee, a set of 8 high speed cameras was used to determine the position of the robot, and to control its motion through the split-actuator design[2]. Other methods of control, utilize position or velocity as an input signal for a feedback loop that simulates insect muscle morphology[4]. As the need for power and control authority onboard flying robot grows, a novel solution to the problem of having to use very large systems to monitor the flight of the robot, is to utilize its wing velocity to simulate insect muscle dynamics, and thereby enable flight with potential capabilities for collision recovery and higher energy efficiency during hovering.

PEAs have been shown to be capable of being used as a self-sensing actuator[23]–[27], with capabilities for removing the need for excess sensor mass on a micro-scale flying robot, where any mass can severely inhibit flight time and energy capabilities. The velocity of a tri-morph piezoelectric actuators has been estimated in situ, utilizing a current sensing circuit and an algorithm to map the sensed current to the velocity of the actuator. The basis of this method relies on the idea that there exists a mechanical current that flows out of the actuator that has a relationship to the strain of the actuator. In this sense, the current is a measure of the change in shape of the actuator.

While some solutions to the problem of concomitant velocity sensing in PEAs require external circuitry that separates the input current from the mechanical current of the PEA[28], [29], solutions that do not require excess hardware are of particular interest for FWMAVs. Models of concomitant sensing that utilize knowledge of the state of the piezo and can return the velocity of the actuator tip with only an input of current through the actuator[30]–[32], are beneficial as they do not require excess circuitry to physically separate the mechanical current. In this research we utilize such a solution to calculate the velocity of a piezoelectric actuator using an input of current that contains information from both the input signal and the mechanical response of the actuator.

To model and solve for the sensed current through the actuator, the piezoelectric tri-morph is simplified into an RC circuit[33] as shown in Figure 5.

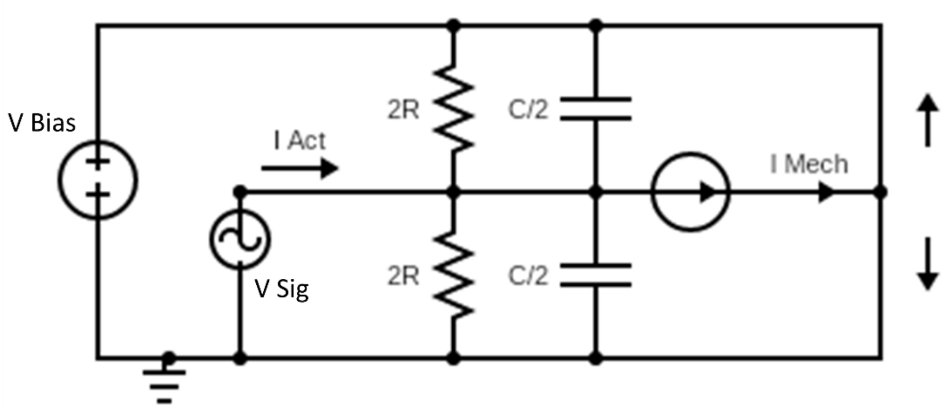

Figure 5. Trimorph Piezoelectric Actuator Electrical Circuit

Here a current, I_{act}, flows through the carbon fiber signal layer and is converted into I_{mech}, which is the mechanical current generated by the actuator related to an exhibited strain. I_{mech} has been found to be a function of the resistance and capacitance of the piezoelectric layers as well as the frequency of the input signal and the material properties of the actuator.

Applying Kirchoff's law, the current draw from the actuator can be shown to be:

$$I_{Act} = \frac{2V_{Sig} - V_{Bias}}{2R} + C\dot{V}_{Act} + I_{Mech}$$

Where I_{Mech} has a linear relationship to velocity that can be described with a coefficient K, such that:

$$I_{Mech} = Kv(t)$$

Solving for velocity we arrive at:

$$v(t) = K^{-1}\left(I_{Act} - \frac{2V_{Sig} - V_{Bias}}{2R} - C\dot{V}_{Act}\right)$$

To measure the actuator current, Op-amps and resistors can be added to the actuator circuit to create a low power consumption current sensing circuit as shown in Figure 6. In the circuit, the actuator current I_{act} runs across the shunt resistor R_S and that current can be measured by knowing the values of $R_1, R_2,$ and R_S.Calculating for I_{act}:

$$I_{Act} = \frac{V_{Sig} - V_{Act}}{R_S} - \frac{V_{Act}}{R_1 + R_2}$$

It must be noted that the resistances and capacitances of the piezoelectric actuator are functions of both bias voltage and frequency of motion, and have been shown to decrease with increasing bias voltage and signal frequency. To minimize computation efforts in determining the frequency of the actuator real-time, the resistance and capacitance values can be chosen to be close to values near or at 1Hz operations. By doing so, the concomitant velocity sensing circuit will not have dependence on the bias voltage and frequency of motion, and will deviate to some extent from the true velocity of the system as the frequency of motion of the actuator increases.

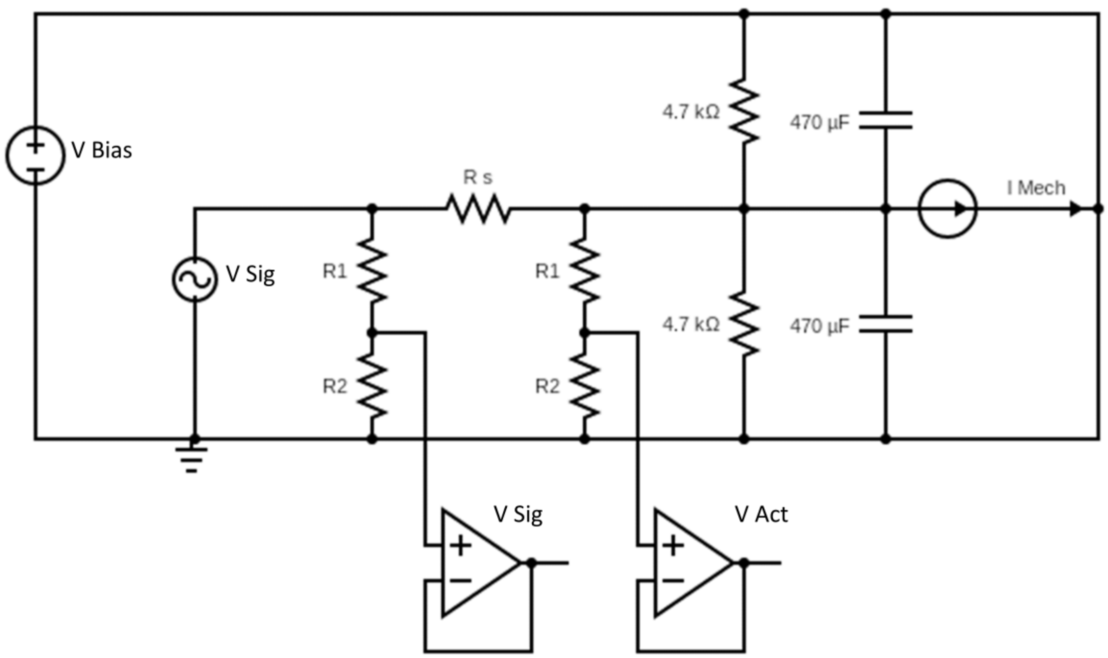

Figure 6. Actuator Model with Op-Amps and Resistors for Current Sensing

Solving for I_{Mech} we arrive at:

$$I_{Mech} = I_{Act} - \frac{2V_{Sig} - V_{Bias}}{2R} - C\dot{V}_{Act}$$

Next, a scalar term, the blocking factor, denoted β is introduced to adjust the mechanical current's phase with the phase of the actuator's velocity as the frequency of the actuator deviates further from resonance. This blocking factor has been shown to improve the calculation of velocity and is likely required due to errors in the measurement of the dielectric properties of the actuator under a fixed state [33]. A value of $\beta = 1.57$ was chosen per previous experiments performed by Jayaram et al. [33]. The current is then denoted as the "Sensed" current and denoted:

$$I_{Sen} = I_{Act} - \frac{2V_{Sig} - V_{Bias}}{2R} - \beta C\dot{V}_{Act}$$

Lastly, a conversion is performed to change the sensed current into units of velocity. It has been found that the relationship between the sensed current and the velocity is linear. Thus, a scalar term α is incorporated to convert the sensed current into velocity in mm/s. Alpha is chosen to be approximately 500 Amm/s from previous studies [33]. The final form of the concomitant velocity equation can then be shown as:

$$v(t) = \alpha\left(I_{Act} - \frac{2V_{Sig} - V_{Bias}}{2R} - \beta C\dot{V}_{Act}\right)$$

Chapter 1 is currently being prepared for submission for publication. Lan, Edward; Lynch, James; Gravish, Nicholas. “Controlled Flight of a Bioinspired Flapping Wing Robot with Asynchronous Control”. The thesis author was the principle researcher/author on this paper.

CHAPTER 2: DESIGN AND FABRICATION OF A FLAPPING-WING ROBOT

SECTION 2.1 DESIGN AND FABRICATION SETUP

The design intent of the robot developed in this research was for it to be designed and fabricated as a platform for the study of insect flight muscle control systems such as the DSA muscles that allow for asynchronous flight. To this end a scaled-up system of the Harvard RoboBee was designed, named the Upscaled RoboBee, with a single piezoelectric actuator, based on designs of the Harvard MoBee. Components were fabricated using the Pop-Up MEMs method of fabrication and were designed to have an approximate scaling of 2X wing size, 3X force generation in the piezoelectric actuator. Components included a trimorph piezoelectric actuator, a folded transmission, passive pitch hinges, mylar wings, and a carbon fiber frame.

Another key component of the robot design was implementation of the robot on a vertical rail guide for decoupled flight testing. A thin wire vertical rail system was developed to decouple vertical lift from rotational pitch, yaw, and roll during flight. Due to a lack of asymmetric control in the robot, lift generation was limited to control of the flapping frequency of both wings together. Through iterative design, the robot's mechanical properties were tuned to allow for properly phased wing pitch to wing stroke motion.

Cutting of all parts was performed on a diode-pumped solid state (DPSS) laser from Photonics Industries. The DPSS laser has a line-cutting precision on the micrometer scale. Different laser power settings and number of laser passes are chosen for varying materials to ensure precise cutting without damaging the material to be cut. For materials such as the thermal adhesive and the Piezoelectric (PZT) ceramic layers, heat is a large factor to creating a good cut. Too high of a heat and the adhesive can burn, or the PZT can hits its curie temperature and depolarize, thereby removing its capability for exhibiting strain under electrical load.

The final configuration of the robot was a 0.200-gram robot with a 7.5cm wing length as seen in Figure 7. The following sections will discuss the design and fabrication of each individual component.

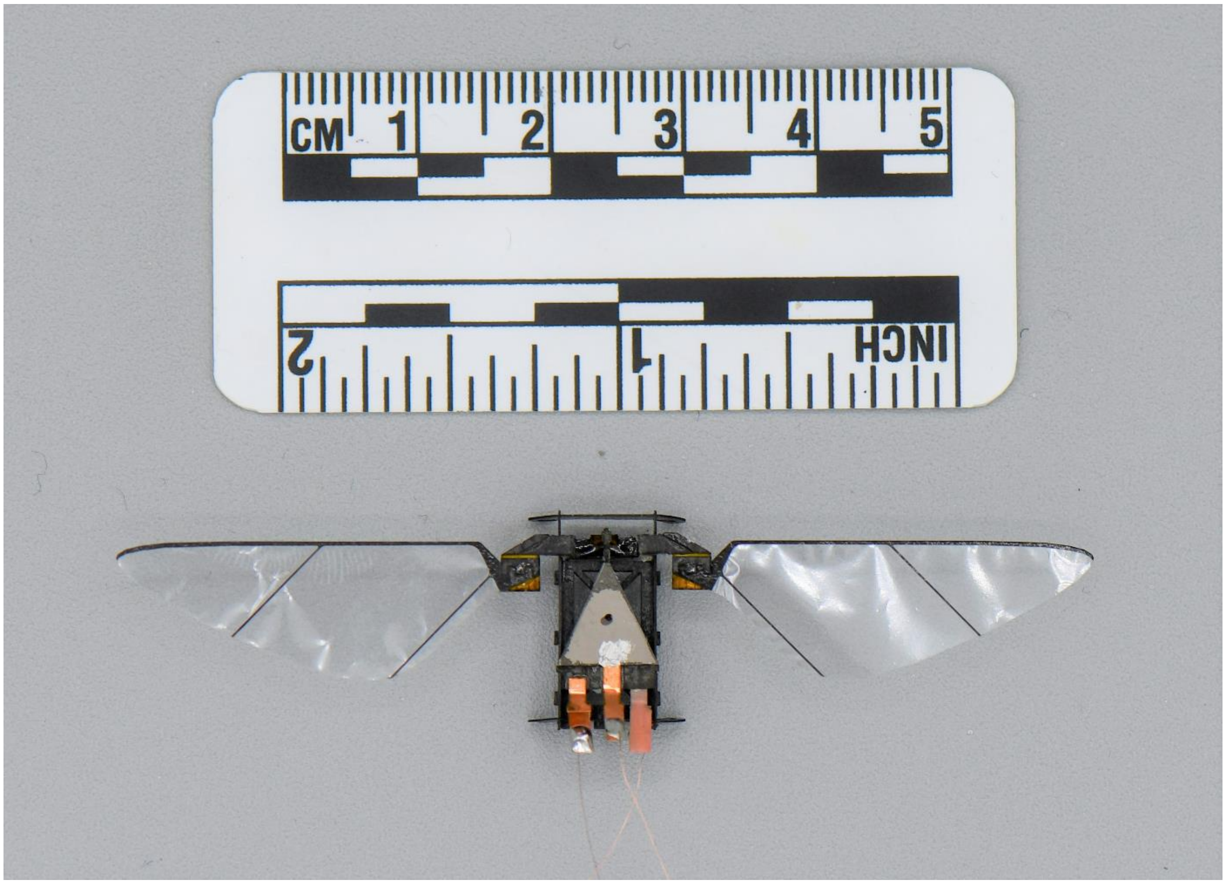

Figure 7. Upscaled RoboBee with Ruler for Scale

SECTION 2.2 PIEZOELECTRIC ACTUATOR

The piezoelectric actuator was designed as a trapezoidal trimorph actuator with 2 layers of piezoceramic sandwiching a layer of unidirectional carbon fiber. The top and bottom of the actuator are tipped with non-conductive fiberglass to minimize conduction paths and to add stiffness and increase deflection of the actuator tip. Copper-clad polyimide film leads, as seen in Figure 8, were co-bonded to the actuator structure to allow for easily solderable pads for which to solder 40 AWG electromagnetic wire. Two-part silver-infused conductive epoxy was utilized to connect copper leads to the top-most and bottom-most layers of the actuator. The silver epoxy bridged the conductive gap due to the stack up of materials from actuator manufacturing. The thermal adhesive and polyimide film generated an insulative barrier that prevented electrical contact between the copper pads and the piezoelectric layers at the top-most and bottom-most layers. The central layer of copper was co-cured using a pre-impregnated unidirectional carbon fiber (pre-preg) and was thus electrically connected to the carbon fiber layer to provide a signal voltage line.

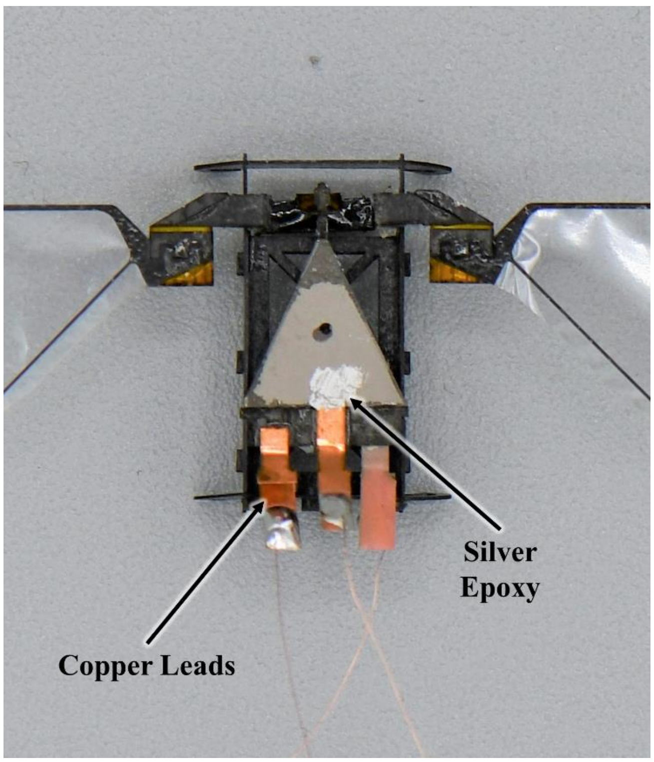

Figure 8. Co-bonded Copper Leads Minimize Manufacturing Steps. Silver Epoxy Provides Electrical Conductivity from the Leads to the Piezoceramic

The manufacturing process began by cutting un-cured [90/0/90] laminate made from M55J unidirectional pre-preg. Laser cutting settings for each layer of the piezoelectric actuator can be found in

Table *1*. Next the piezoelectric ceramic plates were cut, being careful not to exceed the curie temperature of the material and risk depolarization of the ceramic. The ceramic was marked with an alcohol-based ink to identify the polarization direction during the heated press and laser cutting operations. Layers of copper clad polyimide film were cut to provide soldering pads sufficiently far away from the silver epoxy application zones to prevent epoxy thermal failure during the soldering step. Finally, Fiberglass plates (FR4) of 0.005" thickness were cut into sections for the tip and base of the actuator as well as the alignment jig. The cut fiberglass jigs were sprayed with a release agent, Frekote 700-NC. After all individual layers, except for the uncured carbon fiber, had been cut, they were cleaned using an ultrasonic cleaner for 3 minutes in rubbing alcohol, and then air dried until all alcohol had evaporated.

Special care was taken into cleaning the edges of the PZT material. The edges were scrubbed in one direction with a microfiber tip to remove excess PZT dust and debris. Loose substrate, if left on the part, would create a potential leak path for the charge on the piezoelectric layers to jump across while the actuator is under electrical load. This would result in sparking that could burn and damage the actuator.

Once all materials were sufficiently cleaned of manufacturing debris, the layers were stacked using alignment pins and a fixture plate. The stack up was then placed in a heated press under approximately 30 psi at 350°F for 2-3 hours. When the cure had finished and the part had sufficiently ramped down in temperature to below 150°F, pressure was removed and the cured stack up was demolded. The actuator stack up was then processed to generate the final release cuts and remove excess materials.

Table 1. DPSS Laser Cutting Settings for Pre-Stack Materials

Material	**Thickness (mm)**	**Laser Frequency (Hz)**	**Laser Power (%)**	**Number of Passes**
M55J Carbon Fiber Pre-Preg	0.053	12000	100	10
YLA RS-3C Carbon Fiber Pre-Preg	0.027	12000	100	5
Polyimide Film	0.01	12000	100	2
Copper Clad Polyimide Film	0.0354	12000	100	15
Copper Shim	0.0254	12000	100	10
[0/90/0] Carbon Fiber	0.08	12000	100	15
[0/90/0] Carbon Fiber	0.16	12000	100	30
Pyralux LF1500	0.01	12000	25	2
PZT-5H	0.053	12000	15	2500
FR4	0.053	12000	100	25

SECTION 2.3 TRANSMISSION

The transmission was comprised of stiff carbon fiber links and compliant polyimide film pivot points which acted either as a fold location that could be rigidized with cyanoacrylate glue and solder, or as a hinge joint. A top layer of copper was added to allow for a rigid solder joint in locations where cyanoacrylate glue had a higher probability of fatigue and catastrophic failure. In locations where the copper pads were not sufficiently large due to the geometry of the part, cyanoacrylate glue was used to fuse the joints into 90° bends. Implementation of the solder pads also allowed for the use of reflow solder, such that the transmission could be fit into a precision jig, and solder paste applied to rigid joints on the carbon fiber links at room temperature. When heated, the solder paste would liquefy and fuse to the copper pads, which, when placed along 2 sides of a folded joint, would solidify the bend point.

The transmission was designed as a kinematic joint, translating the actuator tip deflection along the horizontal plane into wing stroke rotation about the robot's vertical axis, as seen in Figure 9.

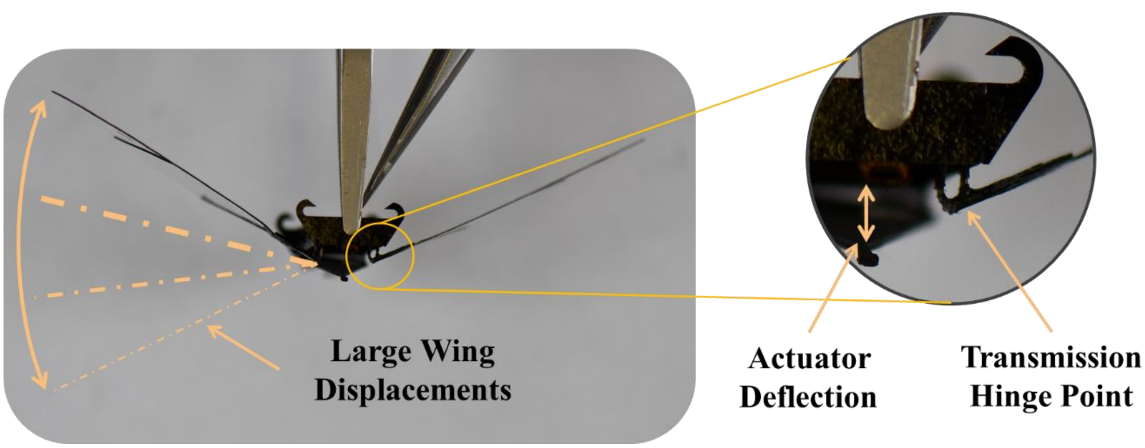

Figure 9. Deflection of the Actuator is Translated into Rotational Motion in the Wing Stroke Through a Compliant Transmission

The transformation of the actuator tip deflection into the wingtip angular displacement was derived from the kinematics of the system as seen in Figure 10.

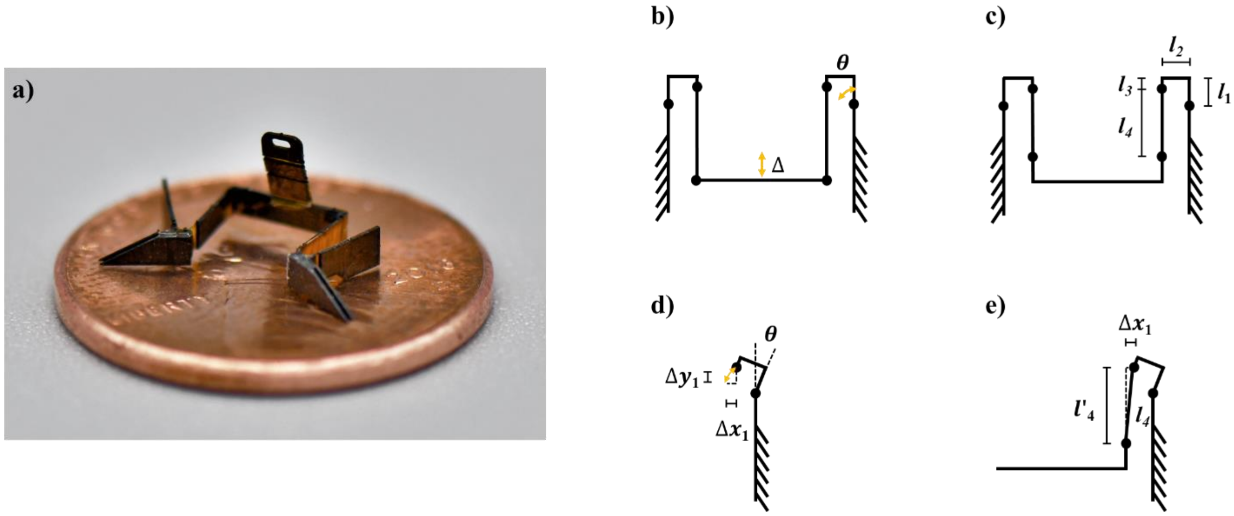

Figure 10. The Transmission Kinematics - a) Folded Transmission on penny for scale b)-e) Kinematics Diagrams Showing Dimensions and Kinematic Relations

$$\Delta x_1 = l_2 - cos\theta\sqrt{{l_2}^2 + (l_1 - l_3)^2}$$

$$\Delta y_1 = cos\theta\sqrt{{l_2}^2 + (l_1 - l_3)^2} - (l_1 - l_3)$$

$$l'_4 = \sqrt{{\Delta x_1}^2 + {l_4}^2}$$

$$\Delta = \Delta y_1 + l_4 - l'_4$$

Due to the nonlinearity of the kinematics, however, an approximation is taken such that the transmission ratio is approximately equal to $T \equiv \frac{\theta}{\Delta} \approx \frac{\theta}{l_2}$. This approximation was taken as a general design estimate, reducing the need for performing rigorous numerical calculations of the actuator displacement to wing angular displacement.

SECTION 2.4 HINGE

The hinges of the robot allowed passive pitching of the wing through a layer of compliant polyimide film and were designed to provide a maximum total pitch sweep angle of 140°. Design for manufacturing considerations were made for fabrication of a hinge that would easily slot into the transmission and allow a wing to be easily aligned and attached. A thickness of 0.01mm polyimide film was chosen to allow proper passive wing pitching during the stroke of the flapping wing. The pitch angle was derived based off the geometry of the compliant hinge and carbon fiber section as shown in Figure 11. Utilizing the design as shown, the wing provided a maximum pitch angle of 70° relative to the vertical axis of the robot.

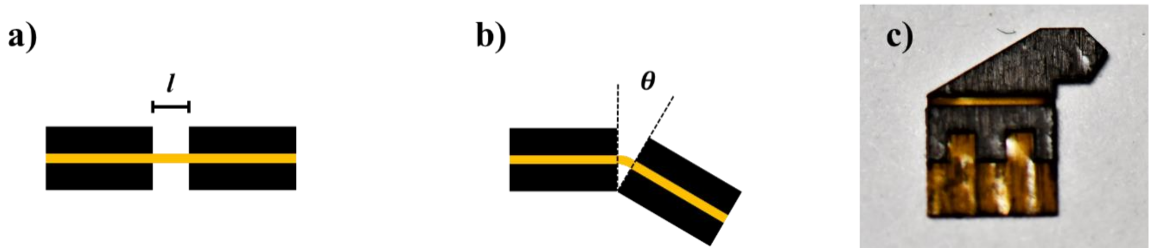

Figure 11. a) Passive Pitch Hinge Diagram with open spacing l b) Diagram of Fully Bent Hinge at angle θ c) Final Release Cut Hinge

SECTION 2.5 WINGS

The wings were designed to mimic the shape of bee wings in shape and were scaled to approximately 2X the Harvard RoboBee wing size. To fabricate the wings, a thin layer of adhesive film was applied onto a [0,45,0] pre-cured carbon fiber stack up. The stack up was then cut using the DPSS laser to generate wing spar geometry. The 45° fibers were aligned with the direction of the 45° wing spars to provide stiffness as shown in Figure 12. Once the internal sections of the spar cut were removed, a layer of 0.01mm thick mylar film was laid over the stack up and adhered to the film adhesive. A final release cut was then performed to generate the final feature geometry for the mylar wing.

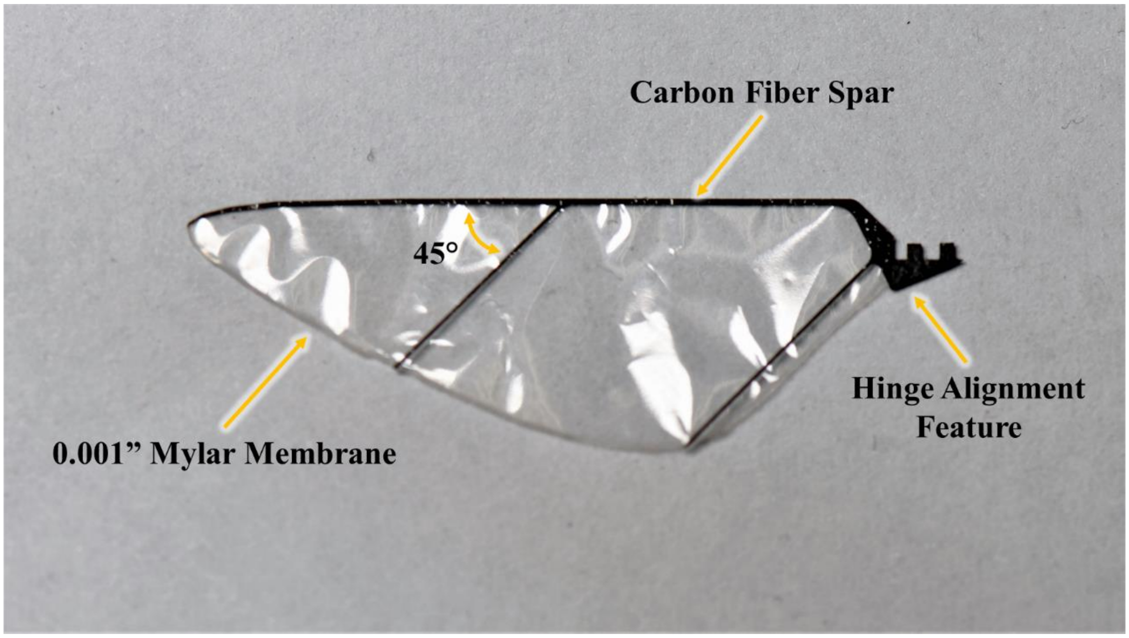

Figure 12. Mylar Membrane Wing with Carbon Fiber Spars and Hinge Alignment Feature

SECTION 2.6 FRAME

The carbon fiber frame was designed for easy assembly with slots to fit and lock the truss frame together. Using a [0/90/0] 160um thick pre-cured stack up, the frame pieces were laser-cut and assembled using cyanoacrylate glue to bind the slotted joints together. Guide rail hooks on the upper and lower cap of the frame of the robot allow for attachment to a vertical rail system for flight testing as seen in Figure 13.

Figure 13. The Upscaled RoboBee Sits On a Vertical Rail System With Copper Wires Acting as Low Friction Guides

The frame stood approximately 20 mm tall and had a total weight of 0.050g, making up 25% of the overall mass.

CHAPTER 3: CONCOMITANT SENSING

SECTION 3.1 EXPERIMENTAL SETUP

An experiment was designed to concomitantly sense the velocity of a piezoelectric trimorph actuator through a current sensing circuit. To validate the calculated velocity, a Philtec fiber optic displacement sensor was used to measure the displacement of the tip of the piezoelectric actuator at varying sinusoidal inputs as seen in Figure 14. A layer of mirror-finished steel shim was attached to the tip of the actuator to provide a low-distortion reflective surface for the fiber optic sensor to reflect off. Data acquisition and signal output were controlled by an NI DAQ model PCIE PCIe-6343 through MATLAB Simulink with a sampling frequency of 10,000Hz.

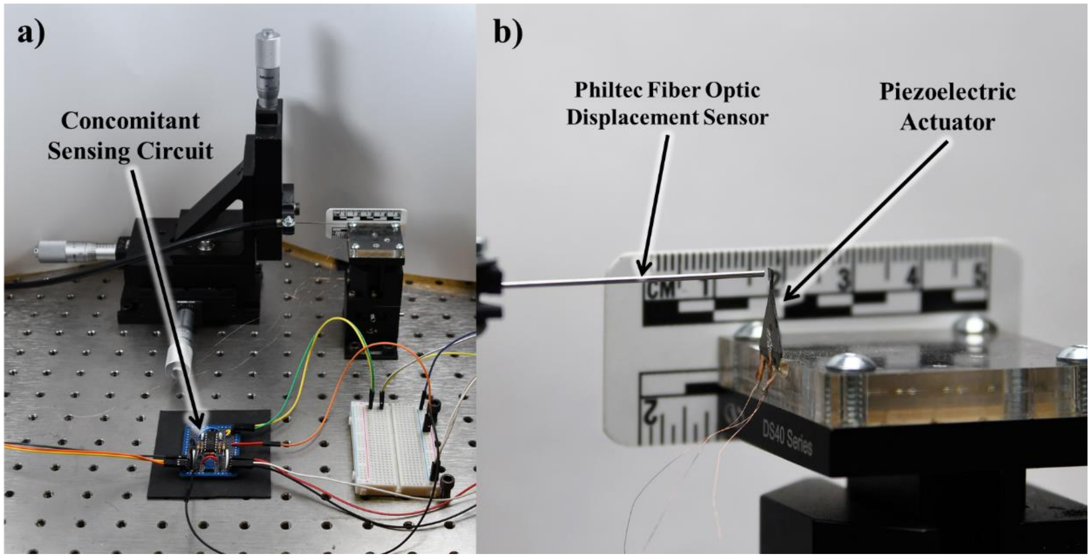

Figure 14. a) Concomitant Sensing Circuit Wiring b) Mounted Piezoelectric Actuator with Fiber Optic Displacement Sensor for Concomitant Sensing Validation

SECTION 3.2 ACTUATOR CHARACTERIZATION

Characterization of the frequency response of the piezoelectric actuator was performed to determine the natural resonant frequency of the actuator using a swept-sinusoidal chirp input. The swept sinusoidal signal started from 0Hz and increased to 2500 Hz across a 20 second time-span. A 2 second ramp up and ramp down were incorporated into the chirp signal to minimize fatigue in the piezoelectric actuator due to signal discontinuity. The natural frequency of the actuator was measured to be approximately 2190Hz with a maximum displacement amplitude of 3.5mm and velocity amplitude of approximately 4.8 m/s as shown in Figure 15.

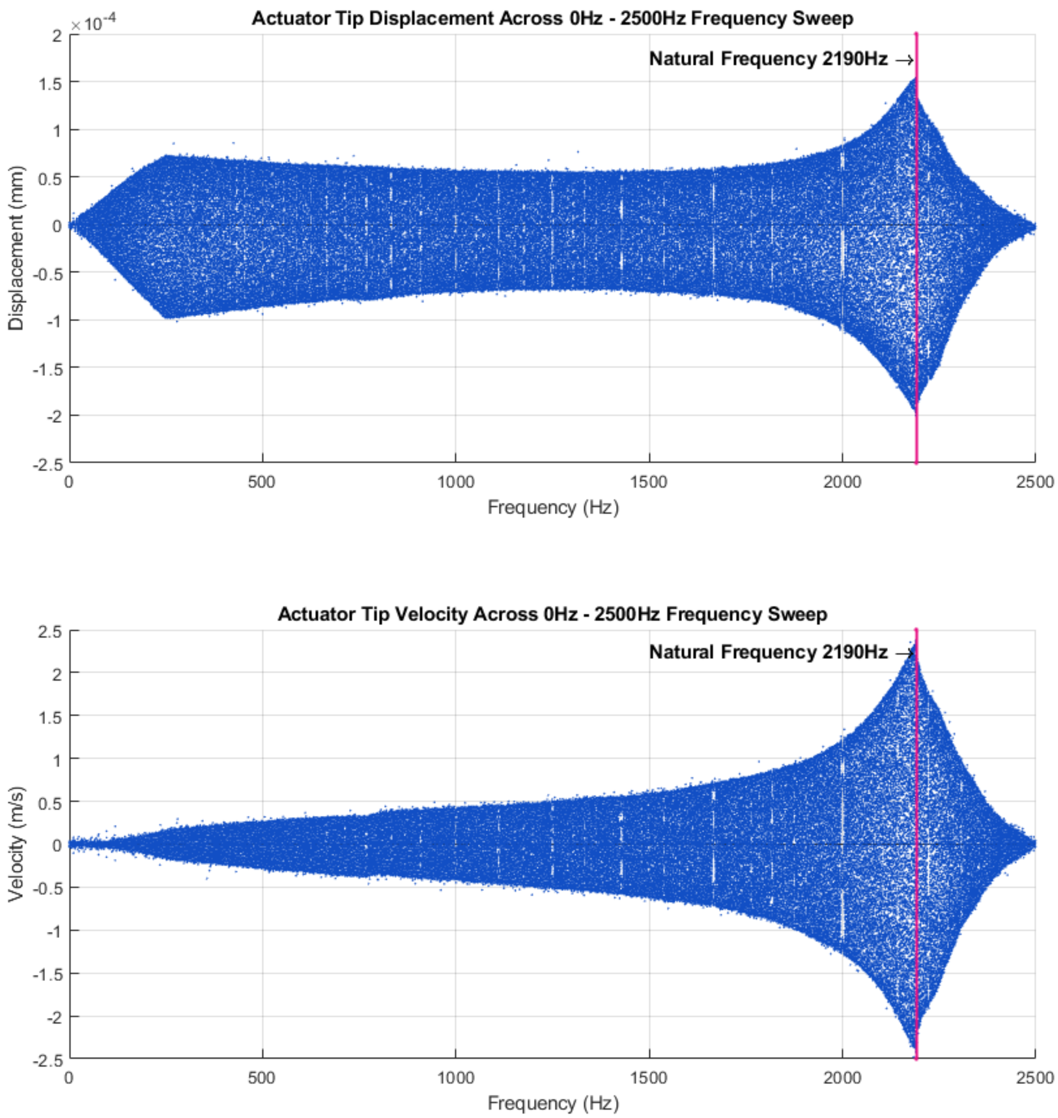

Figure 15. Piezoelectric Trimorph Actuator Frequency Response

SECTION 3.3 VELOCITY SENSING RESULTS

A frequency sweep was performed on the actuator, using a swept sinusoid and calculated values of velocity were compared to measured values from the fiber optic displacement sensor. A 0Hz to 200Hz frequency range was chosen to perform concomitant velocity calculations. This frequency range was chosen because the natural frequency of the robot was far below the 200Hz range. Actuator voltage and signal voltage were recorded and processed through MATLAB. MATLAB Simulink was used to run and store the data in real time.

With an unloaded piezoelectric actuator, the concomitant velocity calculation closely matched the measured velocity of the tip of the piezoelectric actuator. At higher frequencies, the calculation deviated, as seen in Figure 17, which is expected due to the approximation of the resistance and capacitance of the actuator each as a constant coefficient. As the resistance and capacitance values of the actuator decreased with increasing frequency, the concomitant calculation generated a higher velocity than measured, until the actuator reached its resonant point, and the measured velocity exceeded the calculated concomitant velocity.

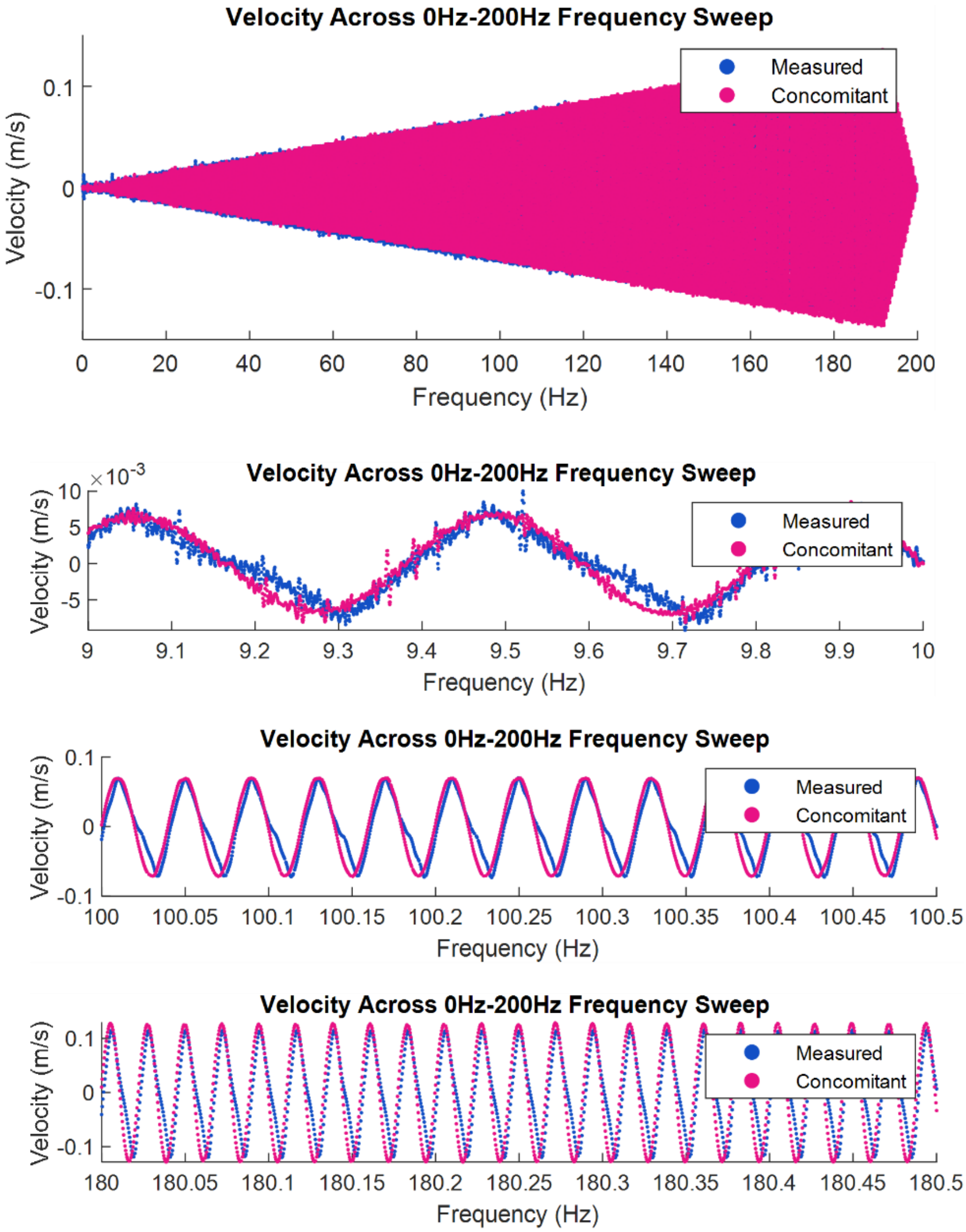

Figure 16. Concomitant Velocity Calculations Across a 0-200Hz Frequency Sweep of an Unattached Piezoelectric Actuator

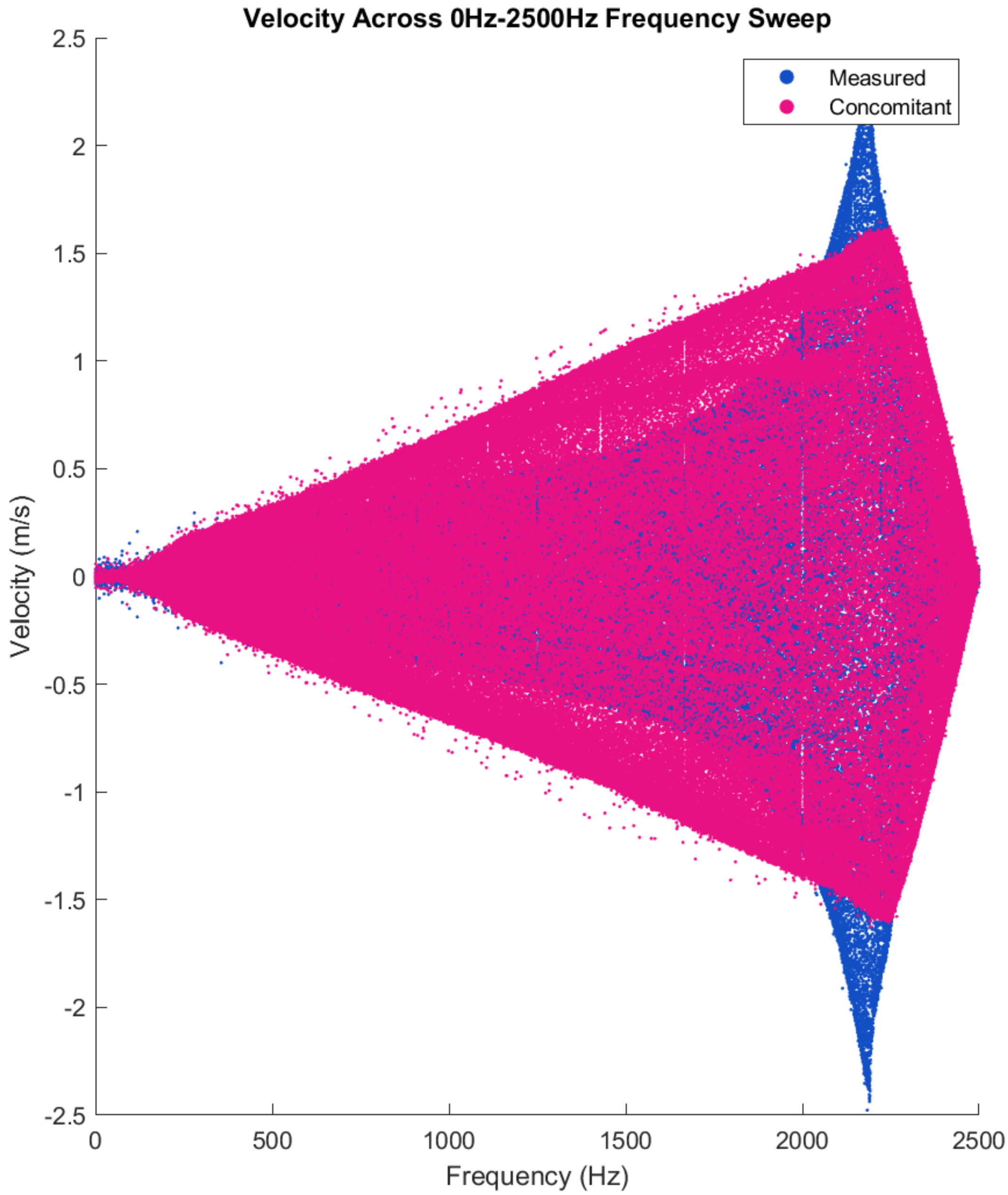

Figure 17. 0Hz to 2500 Hz Concomitant Velocity Frequency Sweep

CHAPTER 4: FLAPPING-WING ROBOT EXPERIMENTATION

SECTION 4.1 EXPERIMENTAL SETUP

To test the natural flapping frequency of the robot and the robot's capability for DSA feedback control, the robot was held in a constrained position with a Philtec Fiber Optic Displacement sensor attached to Thorlabs translation stage, model PT3, to measure the amplitude response of the transmission. A thin sheet of reflective steel shim was attached to the backside of the transmission as shown in Figure 18. A high-speed camera, Phantom VEO 410L was placed above to track the motion of the wing and check for phasing discrepancies between the wing pitch angle and the stroke angle. An NI data acquisitions device, PCIe-6343, provided an output signal and sampled the displacement from the fiber optic sensor at a sampling rate of 1/10000s. Voltage signals were output from a National Instruments BNC-2110 terminal block and amplified using a 250V max piezoelectric amplifier from Piezo Drive, model TD 250. This allowed for bias voltage of 200V, and total potential span from 0V to 200V between Bias line and ground line on the piezoelectric actuator.

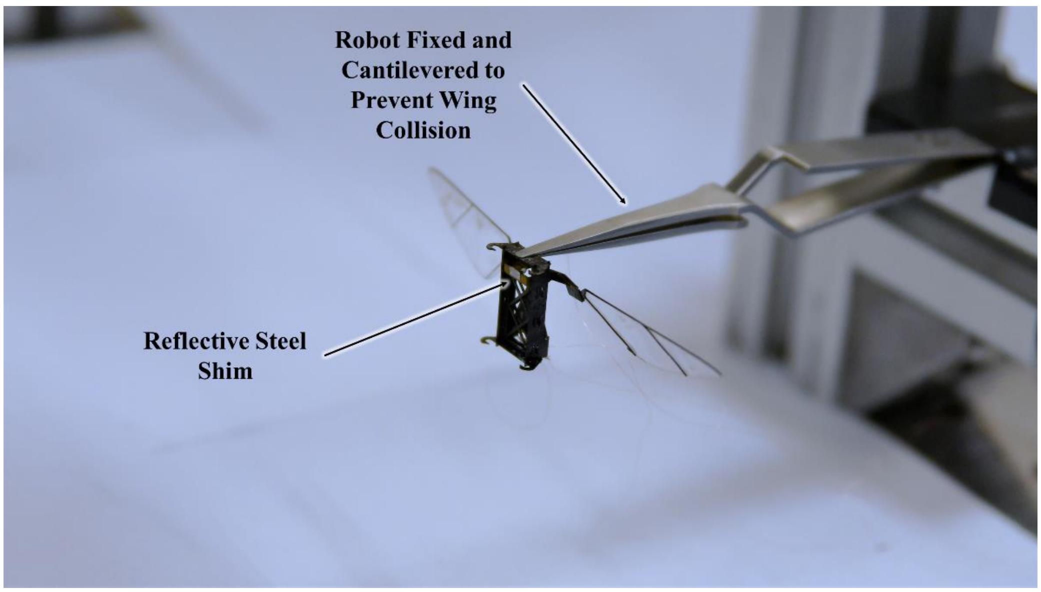

Figure 18. Constrained Flapping Wing Robot Experimental Setup (Displacement Sensor Removed for Clarity)

SECTION 4.2 FLAPPING FREQUENCY SWEEPS

The natural frequency of the robot's flapping wings was found by applying a swept sinusoidal signal of increasing frequency from 0 to 100Hz across 20 seconds with a bias voltage of 200V. The amplitude of the displacement was measured with the fiber optic displacement sensor, and the high-speed camera (1000 fps) was used to capture video to visually check the phase change of the wing pitch relative to the stroke. Maximum amplitude was defined as the maximum displacement of the transmission in which the phase of the pitch of the wing remained synchronous to the phase of the stroke. The natural flapping frequency of the system was found to be approximately 30 Hz. At frequencies above the resonant peak, the pitch phase of the wing became out of phase with the stroke, deviating from the wing motion as described in Figure 19.

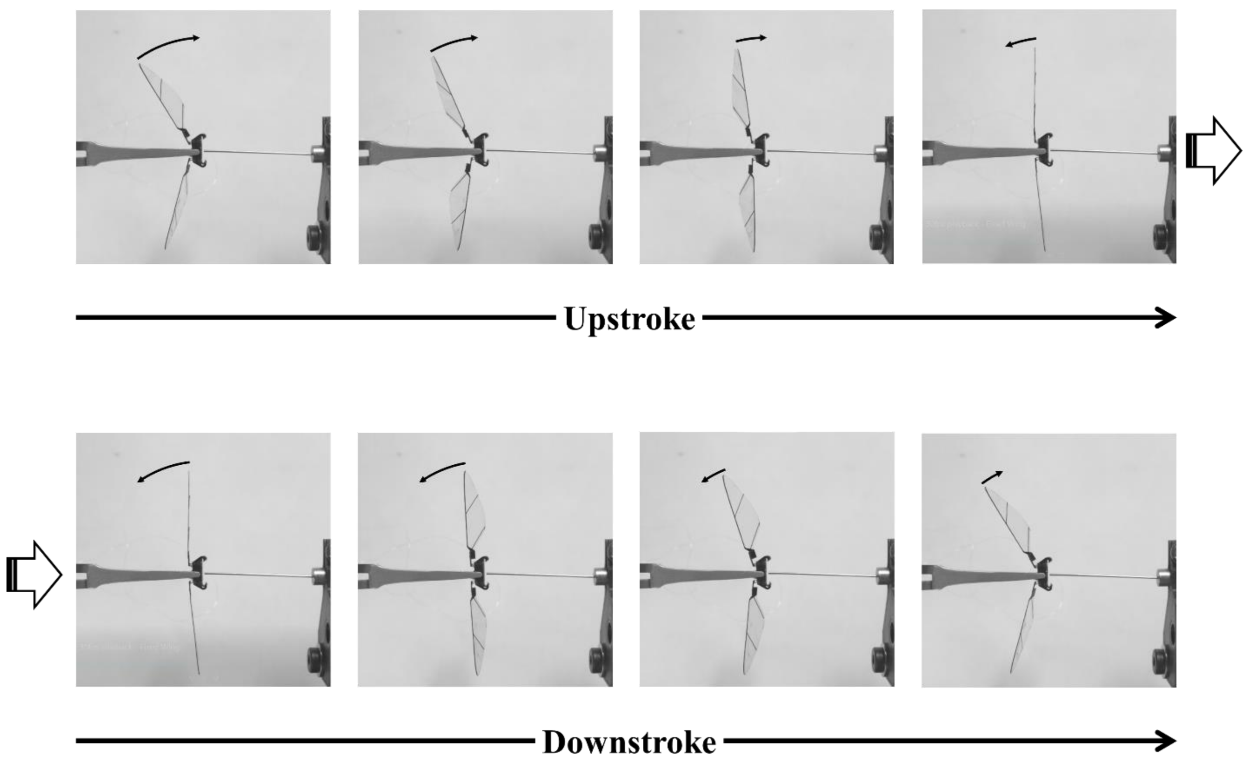

Figure 19. Robot Wing Upstroke and Downstroke Motion

Concomitant velocity calculations were then performed, utilizing an approximation of the actuator resistance and capacitance as a constant value, and matched against the measured velocity response of the frequency sweep. As frequency increased, and the amplitude of the velocity grew into a resonant peak, the deviation between the measured and calculated velocity increased as well, as seen in Figure 20. This was likely due in part to the approximation of the actuator resistance and capacitance as constant values, when at increasing frequencies, the resistance and capacitance of the tri-morph actuator has actually been shown to decrease as a function of the flapping frequency.

This response also suggests that the spring-mass-damper nature of the wings, hinge, and transmission of the robotic system may be generating decoupled motion from the piezoelectric actuator. In this case, the motion of the transmission, could be decoupled from the actuator significantly enough at higher frequencies, to create deviations in the fiber optic sensor data. To alleviate the deviation of accurate velocity in the system, the spring-wing dynamics of the robotic system could be measured and implemented into the equations for the concomitant velocity sensing of the system.

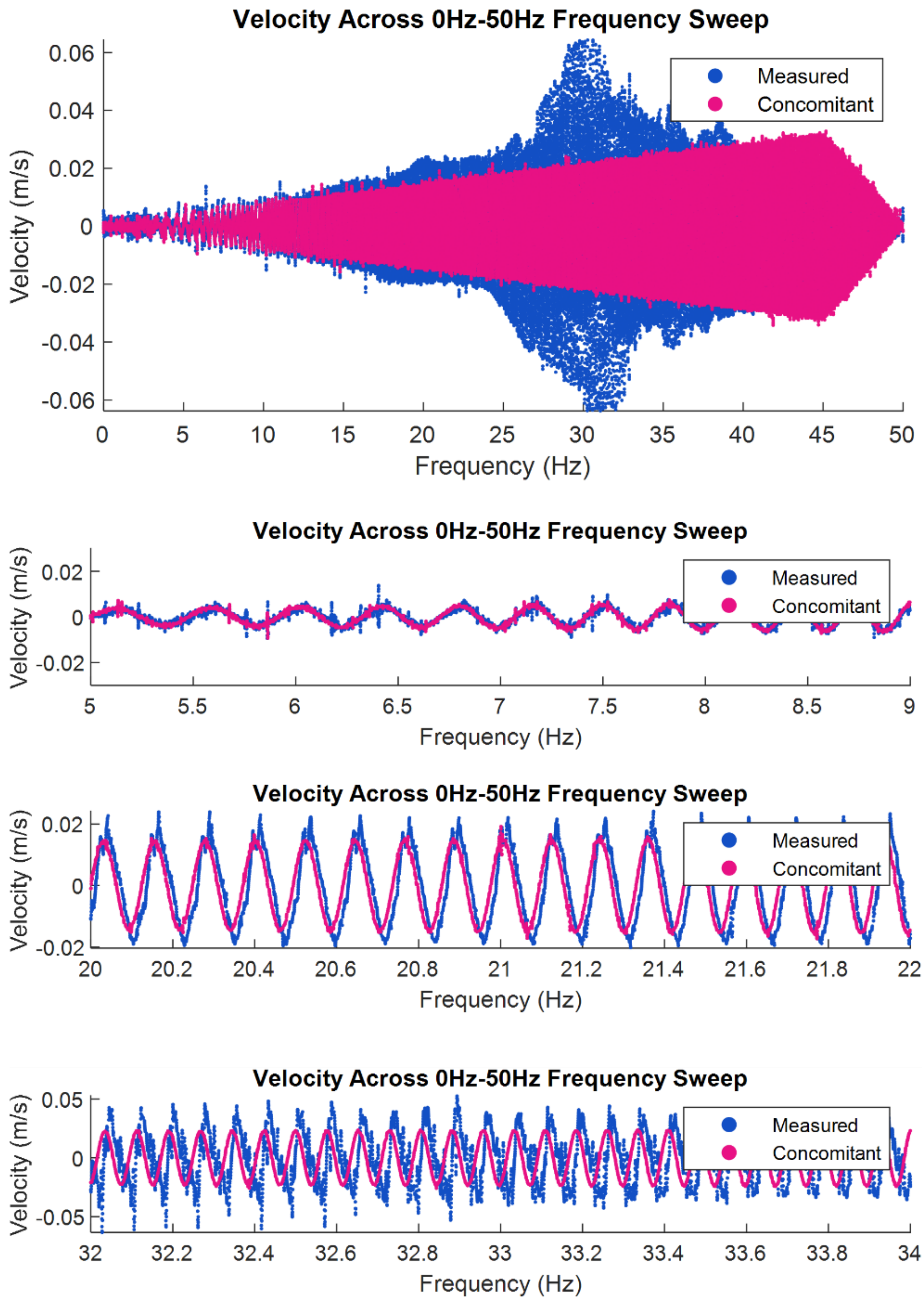

Figure 20. Concomitant Velocity Calculations Vs. Measured Velocity from Fiber Optic Sensor

SECTION 4.3 DSA FEEDBACK IMPLEMENTATION

Using the same experimental setup, a DSA feedback control program was implemented in MATLAB Simulink. The control program provided computation of the output signal given the input of displacement from the fiber optic sensor. Sensor displacement data was run through a low pass filter to prevent incorrect signal sampling, and then differentiated to provide a velocity input into a DSA transfer function block. A transfer function block representing a delay-stretch-activated antagonistic muscle-pair acted as the oscillatory signal generator for the system.

Stable oscillatory modes were found for given values of mu and r3, in which the flapping motion of the wing provided a smooth transition between peaks of stroke amplitude. The range of r3 and mu utilized were on the order of r3 = 130 to 170 and μ = 1.65e5 to 2e5. As can be seen in Figure 21, stable limit cycles began to form around μ = 1.65e5 at r3 = 170, fully stabilizing at μ = 1.79e5 for all values of r3. At values of μ = 1.93e5 and above, small sharp peaks can be seen in the limit cycles, that correlate to an oscillatory jitter at the end of the forward and backward stroke, when the actuator has reached its final position and become saturated, which can be seen in Figure 23, which compares the voltage signal provided to the actuator vs. the measured and calculated velocity of the actuator. At this position, the piezoelectric actuator is saturated, but the transmission and wing system, which act like spring-mass-dampers, continue to move due to their inertia and spring properties.

A second experiment was run utilizing the same setup, but with velocity concomitantly sensed from the actuator current, producing stable limit cycles at r3 and μ ranges comparable to having velocity output from the fiber optic displacement sensor. With concomitant velocity sensing incorporated, stable oscillatory limit cycles were achieved at r3=130 to 170 and μ = 1.51e5 to 2e5 as in Figure 22. Under this method of velocity sensing, the robot was able to achieve limit cycles at lower gains of μ, which was expected due to the damping effects of the compliant transmission. As the concomitant velocity sensing method generates the velocity of the actuator tip, and the compliance of the transmission generates a damping effect on the actuator motion, it is to be expected that the feedback loop implemented with concomitant velocity sensing would be able to generate limit cycles with smaller gains.

Comparing the measured velocity against the concomitantly sensed velocity during the DSA feedback loops, it can be seen that the concomitant velocity tracks well. As seen in Figure 24, a comparison of the measured vs calculated velocities generates a relatively linear 1:1 scaling along a comparison graph. As there is seen to be some phase difference between the two velocities, the curve is not perfectly 1:1, but resembles an ellipse. As seen in Figure 25, we note that as the input signal begins to reach the rails of the ground and bias voltage, and reaches a periodic voltage limit, the concomitant velocity measurement breaks down, as the input signal saturates.

As a final test, the actuator is encased in epoxy to employ a fully constrained boundary condition along the length of the actuator, then a frequency sweep is run and the concomitant velocity calculated. As can be seen in Figure 26, the concomitant velocity is shown to break down under these conditions, which we expect due to the simplification of resistance and capacitance of the actuator as constant values. Because of this simplification, the concomitant velocity sensing method is unable to fully detect and calculate the loading of the actuator, and instead generates a response due to the input signal voltage. This suggests that for a truly concomitant sensing circuit, it is necessary to perform one of two options in order to sense the application of loads on the actuator. The first option would be to incorporate an electronic circuit to electrically separate the mechanical current signal from the actuator input signal, and allow for reduction of known parameters for the concomitant velocity calculation. The second option, would be to implement a frequency estimator, to estimate the frequency of the system at any given time and then utilize that measurement to calculate the capacitance and resistances of the actuator.

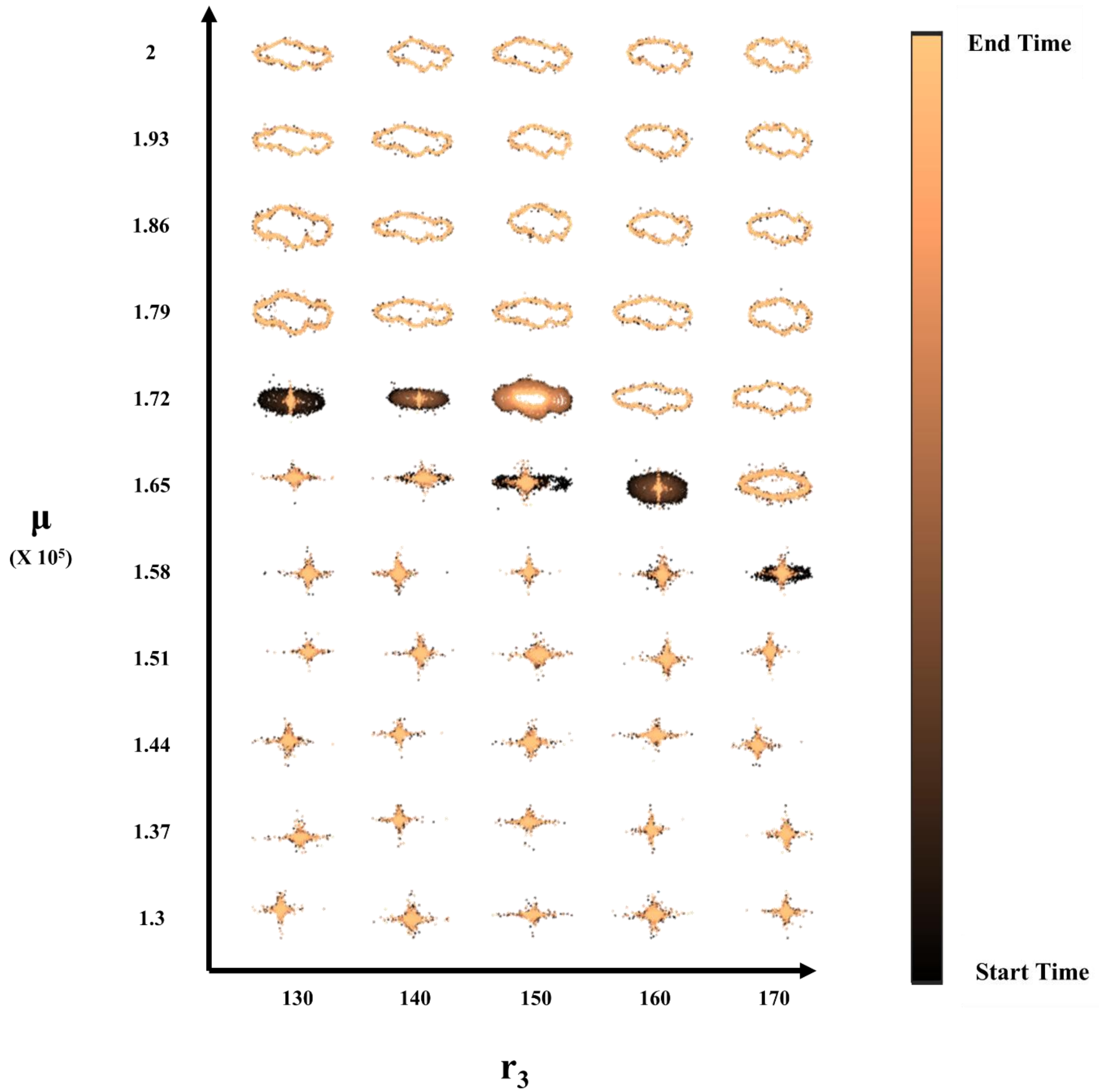

Figure 21. Limit Cycles in Phase Space the Upscaled Robobee Transmission, Using Fiber Optic For Velocity Sensing

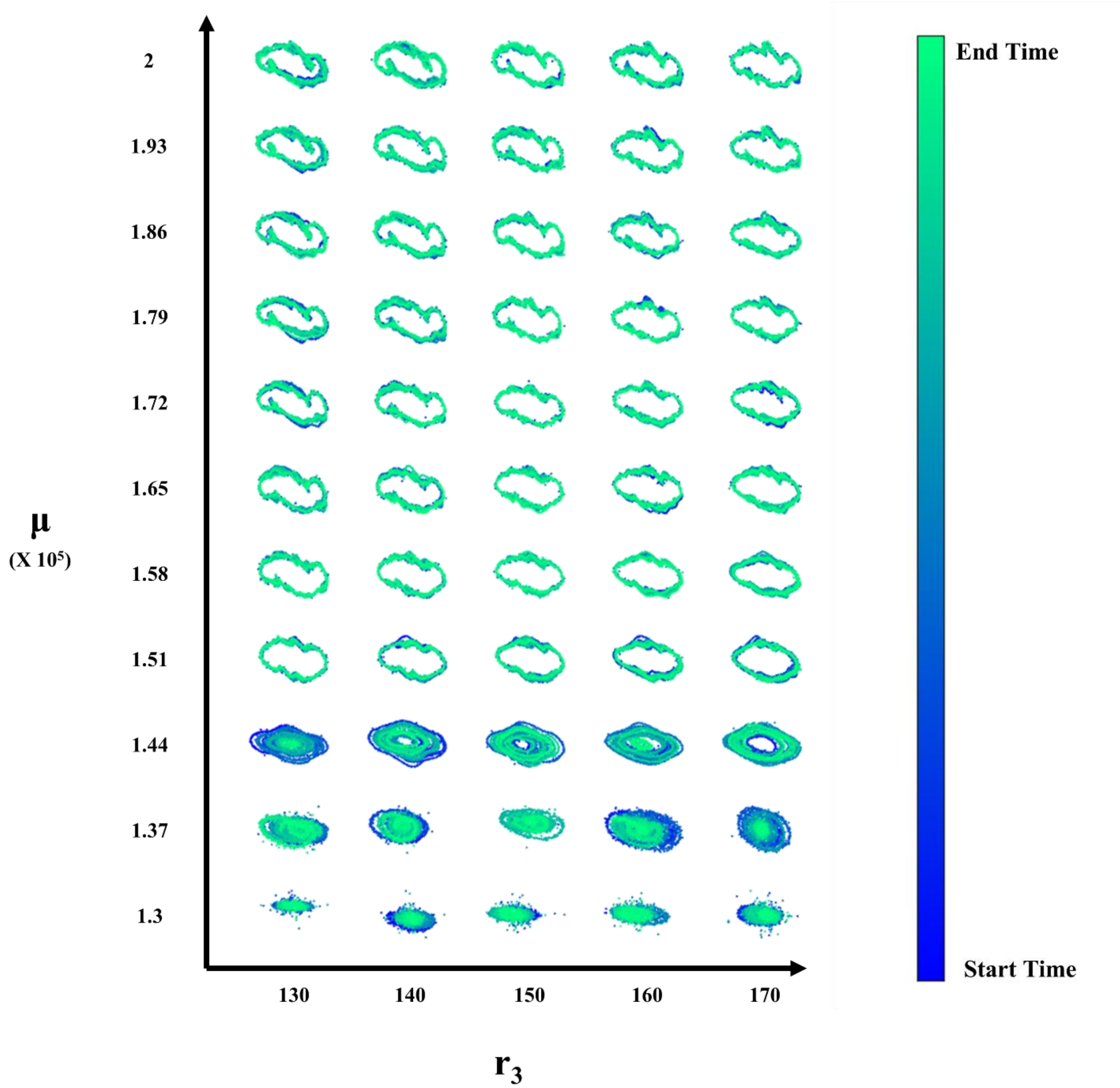

Figure 22. Limit Cycles in Phase Space the Upscaled Robobee Transmission, Using Concomitant Velocity Sensing

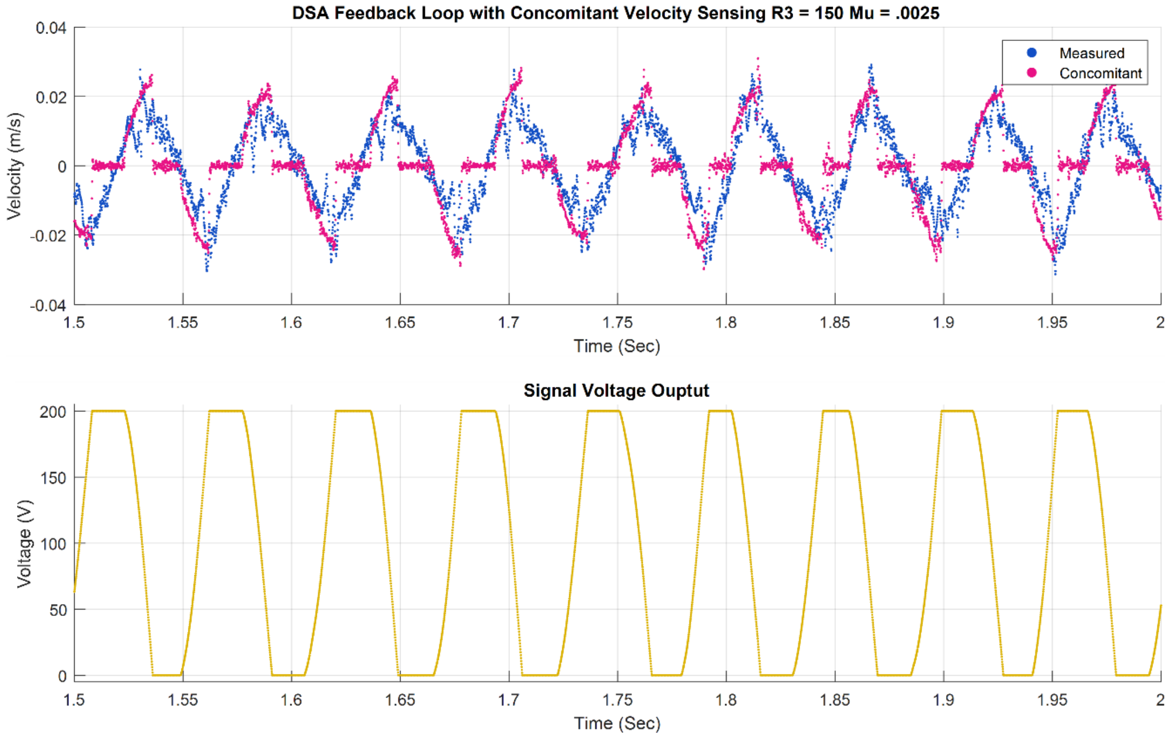

Figure 23. Comparison of Supply Voltage and Velocity from a DSA Feedback Loop with Concomitant Velocity Sensing

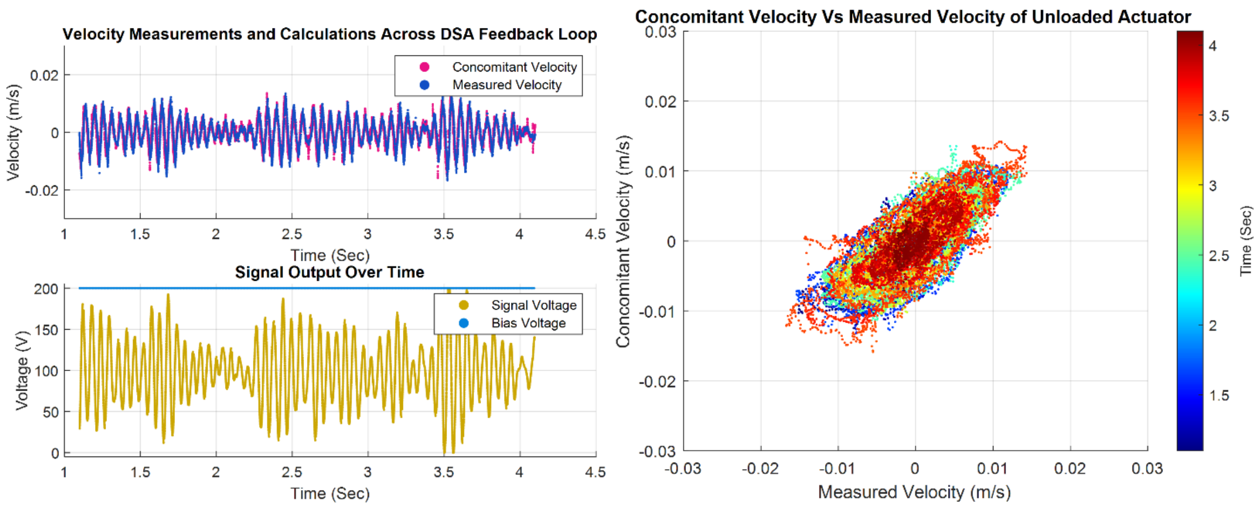

Figure 24. DSA Feedback Loop Comparison of Measured Vs. Concomitant Velocity with no Input Signal Voltage Saturation

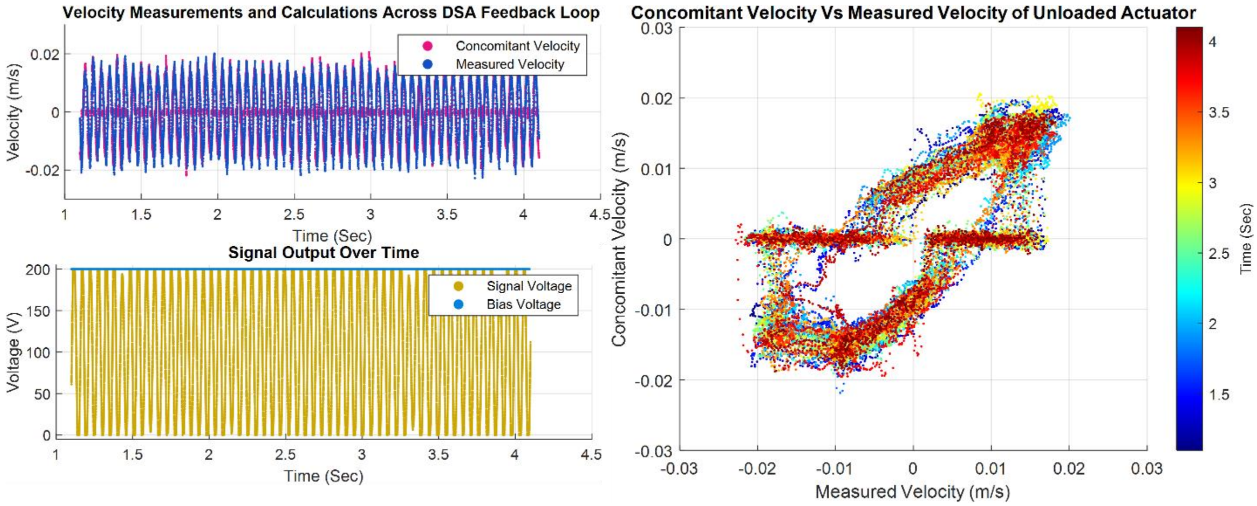

Figure 25. DSA Feedback Loop Comparison of Measured Vs. Concomitant Velocity with Input Signal Voltage Saturation

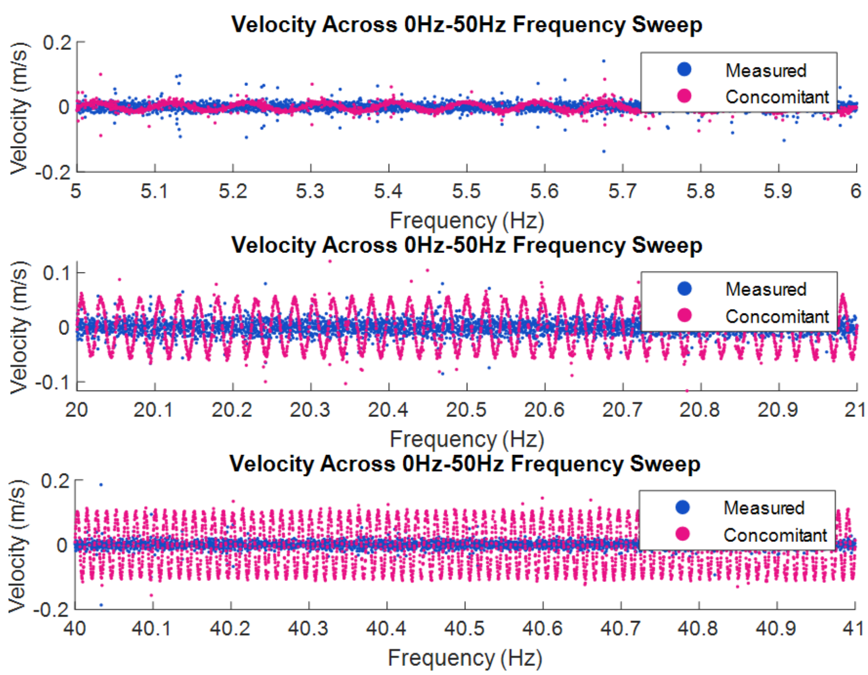

Figure 26. Velocity Sweep of Epoxy-Encased Actuator

CONCLUSION

A bio-inspired flapping wing robot was designed with actuator velocity sensing as a platform for DSA feedback control implementation. The resulting robot utilized a piezoelectric actuator for oscillatory flapping wing motion, and was composed of a carbon fiber frame, with mylar wings. A Pop-up MEMs method was utilized for producing the components, and the overall mass of the robot was 0.200 grams. The wing and transmission mechanisms were designed and built to translate the small piezoelectric actuator tip deflections into large wing rotations with passive wing angle pitching to mimic insect flight.

A circuit was built to measure the output current through the actuator, and a MATLAB Simulink program was designed to retrieve the input and convert it to an actuator tip velocity. The concomitantly sensed velocity measurements were validated using a Philtec fiber optic displacement sensor pointed at the transmission of the robot. The results showed good matching of the velocity with an unloaded actuator from 0Hz to 200Hz. At frequencies above this range, the velocity calculations deviated from the measured values due to an approximation in the concomitant velocity model of a constant resistance and capacitance of the actuator.

The robot showed capabilities for implementation of DSA muscle feedback loops, with stable oscillations generated at about 1.51e5 μ. The concomitant velocity calculations were shown to match well even under a non-uniform loading during the DSA feedback motion. Deviations to the velocity were shown to occur when the actuator encountered either a forced loading or was given a duration of saturated input signal.

Encasing the actuator in epoxy, a frequency sweep showed that the concomitant velocity sensing method did not match under fully constrained boundary conditions. This suggests that the actuator approximation of resistance and capacitance of the system need to be accounted for to properly sense and account for external loading of the actuator. This can be performed as a secondary external circuit, which removes the effects of the input signal or as a more complex mathematical model, which fully describes the state of the actuator.

REFERENCES

[1] Y. Bayiz, M. Ghanaatpishe, H. Fathy, and B. Cheng, "Hovering efficiency comparison of rotary and flapping flight for rigid rectangular wings via dimensionless multi-objective optimization," *Bioinspiration and Biomimetics*, vol. 13, no. 4, 2018, doi: 10.1088/1748-3190/aab801.

[2] K. Y. Ma, S. M. Felton, and R. J. Wood, "Design, fabrication, and modeling of the split actuator microrobotic bee," 2012. doi: 10.1109/IROS.2012.6386192.

[3] B. Geng, Q. Xue, X. Zheng, G. Liu, Y. Ren, and H. Dong, "The effect of wing flexibility on sound generation of flapping wings," *Bioinspiration and Biomimetics*, vol. 13, no. 1, 2018, doi: 10.1088/1748-3190/aa8447.

[4] J. Lynch, J. Gau, S. Sponberg, and N. Gravish, "Dimensional analysis of spring-wing systems reveals performance metrics for resonant flapping-wing flight," *Journal of the Royal Society Interface*, vol. 18, no. 175, 2021, doi: 10.1098/rsif.2020.0888.

[5] M. H. Dickinson and J. R. B. Lighton, "Muscle efficiency and elastic storage in the flight motor of Drosophila," *Science (1979)*, vol. 268, no. 5207, 1995, doi: 10.1126/science.7701346.

[6] C. P. Ellington, "Power and efficiency of insect flight muscle," *Journal of Experimental Biology*, vol. VOL. 115, 1985, doi: 10.1242/jeb.115.1.293.

[7] D. M. Swank, V. K. Vishnudas, and D. W. Maughan, "An exceptionally fast actomyosin reaction powers insect flight muscle," *Proc Natl Acad Sci U S A*, vol. 103, no. 46, 2006, doi: 10.1073/pnas.0604972103.

[8] Z. J. Wang, "Dissecting insect flight," *Annual Review of Fluid Mechanics*, vol. 37. 2005. doi: 10.1146/annurev.fluid.36.050802.121940.

[9] R. J. Wood, "Design, fabrication, and analysis of a 3DOF, 3cm flapping-wing MAV," 2007. doi: 10.1109/IROS.2007.4399495.

[10] N. T. Jafferis, E. F. Helbling, M. Karpelson, and R. J. Wood, "Untethered flight of an insect-sized flapping-wing microscale aerial vehicle," *Nature*, vol. 570, no. 7762, 2019, doi: 10.1038/s41586-019-1322-0.

[11] M. Keennon, K. Klingebiel, H. Won, and A. Andriukov, "Development of the nano hummingbird: A tailless flapping Wing Micro Air Vehicle," 2012. doi: 10.2514/6.2012-588.

[12] R. K. Josephson, J. G. Malamud, and D. R. Stokes, "Asynchronous muscle: A primer," *Journal of Experimental Biology*, vol. 203, no. 18. 2000. doi: 10.1242/jeb.203.18.2713.

[13] D. A. Syme and R. K. Josephson, "How to build fast muscles: Synchronous and asynchronous designs," in *Integrative and Comparative Biology*, 2002, vol. 42, no. 4. doi: 10.1093/icb/42.4.762.

[14] J. P. Whitney, P. S. Sreetharan, K. Y. Ma, and R. J. Wood, "Pop-up book MEMS," *Journal of Micromechanics and Microengineering*, vol. 21, no. 11, 2011, doi: 10.1088/0960-1317/21/11/115021.

[15] S. Russo, T. Ranzani, J. Gafford, C. J. Walsh, and R. J. Wood, "Soft pop-up mechanisms for micro surgical tools: Design and characterization of compliant millimeter-scale articulated structures," in *Proceedings - IEEE International Conference on Robotics and Automation*, 2016, vol. 2016-June. doi: 10.1109/ICRA.2016.7487203.

[16] H. McClintock, F. Z. Temel, N. Doshi, J. S. Koh, and R. J. Wood, "The milliDelta: A high-bandwidth, high-precision, millimeter-scale Delta robot," *Science Robotics*, vol. 3, no. 14, 2018, doi: 10.1126/scirobotics.aar3018.

[17] A. T. Baisch and R. J. Wood, "Design and fabrication of the Harvard ambulatory micro-robot," in *Springer Tracts in Advanced Robotics*, 2011, vol. 70, no. STAR. doi: 10.1007/978-3-642-19457-3_42.

[18] B. Goldberg *et al.*, "Power and Control Autonomy for High-Speed Locomotion with an Insect-Scale Legged Robot," *IEEE Robotics and Automation Letters*, vol. 3, no. 2, 2018, doi: 10.1109/LRA.2018.2793355.

[19] K. Jayaram, J. Shum, S. Castellanos, E. F. Helbling, and R. J. Wood, "Scaling down an insect-size microrobot, HAMR-VI into HAMR-Jr," 2020. doi: 10.1109/ICRA40945.2020.9197436.

[20] K. Y. Ma, P. Chirarattananon, and R. J. Wood, "Design and fabrication of an insect-scale flying robot for control autonomy," in *IEEE International Conference on Intelligent Robots and Systems*, 2015, vol. 2015-December. doi: 10.1109/IROS.2015.7353575.

[21] A. M. Flynn *et al.*, "Piezoelectric micromotors for microrobots," *Journal of Microelectromechanical Systems*, vol. 1, no. 1, 1992, doi: 10.1109/84.128055.

[22] K. Uchino, "Piezoelectric Devices in the Sustainable Society," *Sustainability in Environment*, vol. 4, no. 4, 2019, doi: 10.22158/se.v4n4p181.

[23] M. Bazghaleh, M. Mohammadzaheri, S. Grainger, B. Cazzolato, and T. F. Lu, "A new hybrid method for sensorless control of piezoelectric actuators," *Sensors and Actuators, A: Physical*, vol. 194, 2013, doi: 10.1016/j.sna.2013.01.043.

[24] J. B. Liseli, J. Agnus, P. Lutz, and M. Rakotondrabe, "Self-Sensing Method Considering the Dynamic Impedance of Piezoelectric Based Actuators for Ultralow Frequency," *IEEE Robotics and Automation Letters*, vol. 3, no. 2, 2018, doi: 10.1109/LRA.2018.2794514.

[25] M. N. Islam and R. J. Seethaler, "Sensorless position control for piezoelectric actuators using a hybrid position observer," *IEEE/ASME Transactions on Mechatronics*, vol. 19, no. 2, 2014, doi: 10.1109/TMECH.2013.2250990.

[26] W. Dong, B. Sun, Y. Cui, and Z. Yang, "Study on observer based piezoelectric self-sensing actuator," *Jixie Gongcheng Xuebao/Chinese Journal of Mechanical Engineering*, vol. 38, no. 7, 2002, doi: 10.3901/jme.2002.07.080.

[27] M. N. Islam and R. J. Seethaler, "Self-sensing tracking control for piezoelectric actuators based on sensor fusion," in *Sensors and Smart Structures Technologies for Civil, Mechanical, and Aerospace Systems 2012*, 2012, vol. 8345. doi: 10.1117/12.915369.

[28] J. J. Dosch, D. J. Inman, and E. Garcia, "A Self-Sensing Piezoelectric Actuator for Collocated Control," *Journal of Intelligent Material Systems and Structures*, vol. 3, no. 1, 1992, doi: 10.1177/1045389X9200300109.

[29] V. Giurgiutiu and A. N. Zagrai, "Embedded self-sensing piezoelectric active sensors for on-line structural identification," *Journal of Vibration and Acoustics, Transactions of the ASME*, vol. 124, no. 1, 2002, doi: 10.1115/1.1421056.

[30] J. M. Dietl, A. M. Wickenheiser, and E. Garcia, "A Timoshenko beam model for cantilevered piezoelectric energy harvesters," *Smart Materials and Structures*, vol. 19, no. 5, 2010, doi: 10.1088/0964-1726/19/5/055018.

[31] V. Hofmann and J. Twiefel, "Optimization of a Piezoelectric Bending Actuator for a Tactile Virtual Reality Display," *Energy Harvesting and Systems*, vol. 2, no. 3, 2015, doi: 10.1515/ehs-2014-0055.

[32] V. Hofmann and J. Twiefel, "Self-Sensing with loaded piezoelectric Bending actuators," *Sensors and Actuators, A: Physical*, vol. 263, 2017, doi: 10.1016/j.sna.2017.06.004.

[33] K. Jayaram, N. T. Jafferis, N. Doshi, B. Goldberg, and R. J. Wood, "Concomitant sensing and actuation for piezoelectric microrobots," *Smart Materials and Structures*, vol. 27, no. 6, 2018, doi: 10.1088/1361-665X/aabdf1.